2023

Rapid synaptic and gamma rhythm signature of mouse critical period plasticity

Version	Published version
Citation (published version):	N. Kopell, K.B. Quast, R.K. Reh, M.D. Caiati, M.M. McCarthy, T.K. Hensch. 2023. "Rapid synaptic and gamma rhythm signature of mouse critical period plasticity." https://doi.org/10.1073/pnas.212318212

PNAS RESEARCH ARTICLE | NEUROSCIENCE

Rapid synaptic and gamma rhythm signature of mouse critical period plasticity

Kathleen B. Quast[a,b,1], Rebecca K. Reh[a,b,1,2], Maddalena D. Caiati[a], Nancy Kopell[c,d,3], Michelle M. McCarthy[c,d,3], and Takao K. Hensch[a,b,d,3]

Contributed by Nancy Kopell; received December 24, 2021; accepted November 29, 2022; reviewed by Ralf A. Galuske and Tommaso Pizzorusso

Early-life experience enduringly sculpts thalamocortical (TC) axons and sensory processing. Here, we identify the very first synaptic targets that initiate critical period plasticity, heralded by altered cortical oscillations. Monocular deprivation (MD) acutely induced a transient (<3 h) peak in EEG γ-power (~40 Hz) specifically within the visual cortex, but only when the critical period was open (juvenile mice or adults after dark-rearing, *Lynx1*-deletion, or diazepam-rescued GAD65-deficiency). Rapid TC input loss onto parvalbumin-expressing (PV) inhibitory interneurons (but not onto nearby pyramidal cells) was observed within hours of MD in a TC slice preserving the visual pathway – again once critical periods opened. Computational TC modeling of the emergent γ-rhythm in response to MD delineated a cortical interneuronal gamma (ING) rhythm in networks of PV-cells bearing gap junctions at the start of the critical period. The ING rhythm effectively dissociated thalamic input from cortical spiking, leading to rapid loss of previously strong TC-to-PV connections through standard spike-timing-dependent plasticity rules. As a consequence, previously silent TC-to-PV connections could strengthen on a slower timescale, capturing the gradually increasing γ-frequency and eventual fade-out over time. Thus, ING enables cortical dynamics to transition from being dominated by the strongest TC input to one that senses the statistics of population TC input after MD. Taken together, our findings reveal the initial synaptic events underlying critical period plasticity and suggest that the fleeting ING accompanying a brief sensory perturbation may serve as a robust readout of TC network state with which to probe developmental trajectories.

thalamocortical | parvalbumin | oscillation | *Lynx1* | GAD65

Significance

Critical periods are developmental windows of rapid plasticity and remodeling of brain networks, whose trajectories are not yet fully understood. Here, we identify transient γ-oscillations induced by sensory imbalance in the mouse visual cortex as a signature of rapid TC plasticity, only when these windows are open. Using computational modeling, we explain the origin of these transient γ-rhythms and their role in rewiring TC networks to initiate the precritical to critical period transition. These findings offer a robust noninvasive biomarker of open critical period state with which to probe derailed trajectories of brain development.

Dramatic circuit reorganization is a hallmark of early critical periods (CP) in brain development. Thalamocortical (TC) axon morphology is notably sculpted in response to sensory deprivation. A classic example is the eventual shrinkage of ocular dominance "columns" in the primary visual cortex (V1) to an eye deprived of vision (1). Strikingly, these wholesale arbor changes are slow, and synaptic bouton alterations within them scale with TC arbor size over days of deprivation (2–4). Likewise, the pruning and regrowth of dendritic spines on excitatory pyramidal cells reflect slow proteolytic processes that gradually accumulate over days of monocular deprivation (MD) in parallel with the loss of visual acuity and responsiveness in mice (5, 6). Surprisingly, extracellular spike recordings suggest middle layers of V1 are the least plastic after MD (7, 8). Whether thalamo-recipient layer IV networks are merely passive transmitters of sensory input or play a more decisive role in sculpting higher level cortical networks during the CP therefore remains unresolved.

Local γ-aminobutyric acid (GABA) circuit maturation instead triggers the opening of sensory CPs, which can be manipulated by molecular and genetic factors (9–18). Fast-spiking, parvalbumin-expressing (PV) interneurons in supragranular cortical layers can shift their responsiveness earlier than pyramidal cells within one day of MD (10–12). Such early changes are consistent with the importance of PV-cell network maturation in initiating CP states (9). Notably, PV-cells also play a pivotal role in the generation of γ-band neuronal oscillatory activity (19) and spike-time coordination (20). The emergence of γ-activity in V1 is both age- and experience dependent, maturing at the onset of the ocular dominance CP (21). Here, we reveal a decreased TC synaptic input specifically onto PV+ interneurons in layer IV as the earliest synaptic changes found to date in response to MD. Using mathematical modeling, we further elucidate the likely processes underlying those early changes.

Electroencephalogram (EEG) recording immediately after acute sensory manipulations showed a rapid rise in γ-power that correlated with the open CP state, both in juvenile wild-type (WT) mice and in multiple models of shifted plastic windows. The brief peak in γ-power emerged immediately following MD, gradually rising in frequency and eventually fading out after several hours. To reveal the synaptic consequences of this rapid rise

Author contributions: N.K., M.M.M., and T.K.H. designed research; K.B.Q., R.K.R., M.D.C., and M.M.M. performed research; K.B.Q., R.K.R., and M.D.C. analyzed data; and K.B.Q., R.K.R., M.D.C., N.K., M.M.M., and T.K.H. wrote the paper.

Reviewers: R.A.G., Technische Universitat Darmstadt; and T.P., CNR / Scuola Normale Superiore (Pisa).

The authors declare no competing interest.

[1] K.B.Q. and R.K.R. contributed equally to this work.

[2] Present address: Department of Psychology, University of British Columbia, Vancouver, BC V6T 1Z4, Canada.

[3] To whom correspondence may be addressed. Email: nk@bu.edu, mmccart@bu.edu, or hensch@mcb.harvard.edu.

This article contains supporting information online at https://www.pnas.org/lookup/suppl/doi:10.1073/pnas.2123182120/-/DCSupplemental.

in γ-power, we optimized a TC slice preparation (22) to directly probe thalamic input onto PV+ and pyramidal cells in layer IV of V1 following deprivation. A dramatic decrease in thalamic input onto PV-cells within layer IV was seen as soon as 2 h after MD, while the same input onto nearby pyramidal cells was unchanged. In order to explore the possibility of a functional relationship between the immediate γ-oscillations and the loss of TC-to-PV synaptic strength post-MD, we turned to mathematical modeling of TC circuits.

We hypothesized that an imbalance in excitatory input onto PV-cells following MD, only during the CP, may initiate ING (interneuronal gamma) rhythms that drive plastic changes associated with the effects of MD. PV-cells are known to self-organize to produce an ING when electrical coupling as well as mutual inhibitory connections are present (19, 20). The developmental trajectory of electrical and inhibitory connections between PV-cells coincides with the onset of CP opening (8, 23) suggesting ING networks are functional during the CP. Our models confirm that γ-oscillations readily emerge through cortical ING dynamics during CP states in response to imbalanced thalamic input, and functionally alter the spike timing between TC cells and PV neurons leading to weakening of previously strong TC-to-PV connections. On a slower timescale, our models predict that ING initiates strengthening of previously silent TC-to-PV synaptic connections, causing the rising γ-frequency and eventual fade out of these oscillations observed experimentally.

Over the time course of MD-induced γ-rhythms, the TC-to-PV network transitions from being independent of input statistics to highly dependent on input statistics. Our study identifies the initial synaptic events driven by MD that precede by days the well-known, anatomical TC axonal arbor changes (1–4). Moreover, the concomitant rise in γ-power holds exciting promise as a robust, rapid biomarker of CP state in humans.

Results

Deprivation Triggers a Rapid, Transient Rise in γ-Power Only During the CP. We recorded the EEG from V1 in awake, behaving mice immediately following eyelid closure. In young WT (postnatal day P24-27), a rapid rise in oscillatory activity was observed selectively in the γ-frequency band, centered at 42 Hz (Fig. 1 and *SI Appendix*, Fig. S1). The power increase was transient, rising over the first 20 min post-MD and abating by 2 h (mean duration ± SD = 93 ± 22 min; Fig. 1*B*) – a striking immediate signature of deprivation during the CP. To rule out the impact of isoflurane exposure during the suturing procedure, control animals underwent anesthesia without eyelid suture. No peak in γ-power was observed in this group (mean maximum γ-power for no MD = 0.11 ± 0.04, 12 mice; MD = 0.32 ± 0.05, 14 mice; Figs. 1 *B* and *C* and 2*A*).

Notably, γ-power was not elevated indiscriminately across the brain, as somatosensory cortex recordings showed no increase in γ-power following MD (mean maximum γ-power over S1 = 0.10 ± 0.01, 9 mice; Figs. 1*D* and 2*A*). To determine whether γ-power elevation was driven by sensory input, some mice were immediately placed in a dark chamber after eyelid closure. EEG recordings from V1 commenced 10 min later after recovery from anesthesia in the dark and did not differ from nonsutured controls (mean maximum γ-power for MD in darkness = 0.15 ± 0.02, 10 mice; Fig. 1*E*). Together, these results indicate an imbalanced visual input during the CP leads to a rapid rise in rhythmic activity selectively in V1. To further investigate whether this brief γ-peak is restricted to a plastic window, we recorded EEG from older mice (>P90). There was no difference in γ-power between these adult animals receiving MD and anesthesia only controls (mean maximum γ-power no MD = 0.176 ± 0.021, 10 mice; MD = 0.175 ± 0.037, 12 mice; Fig. 2*A*).

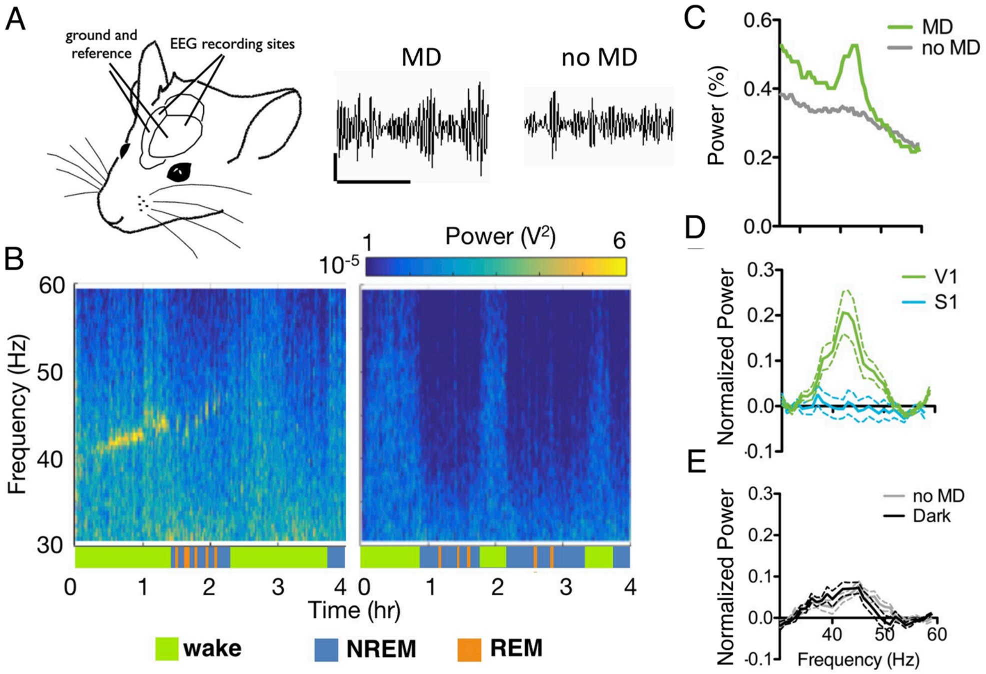

Fig. 1. Monocular deprivation induces a peak in γ rhythm (~40 Hz) during the CP. (*A*) EEG electrodes placed on the surface of the cortex bilaterally over V1, with ground and reference placed anteriorly. EEG traces from V1 with or without MD, band-pass filtered between 30 and 60 Hz. (Scale bar: 200 mV, 500 ms.) (*B*) EEG power spectrum from representative wt juvenile mice following MD (*Left*) or anesthesia (*Right*). Behavioral state indicated by colored bars below plots. (*C*) Average power spectrum during wake for the first 2 h following anesthesia comparing the two mice shown in *B*, as a percentage of total power. (*D*) Mean γ power over V1 for the first hour post-MD (green, n = 14), MD with EEG over S1 (blue, n = 9); *(E)* no MD (gray, n=12) or MD recorded in darkness (black, n = 10). Normalized to NREM γ power, error bars show SEM.

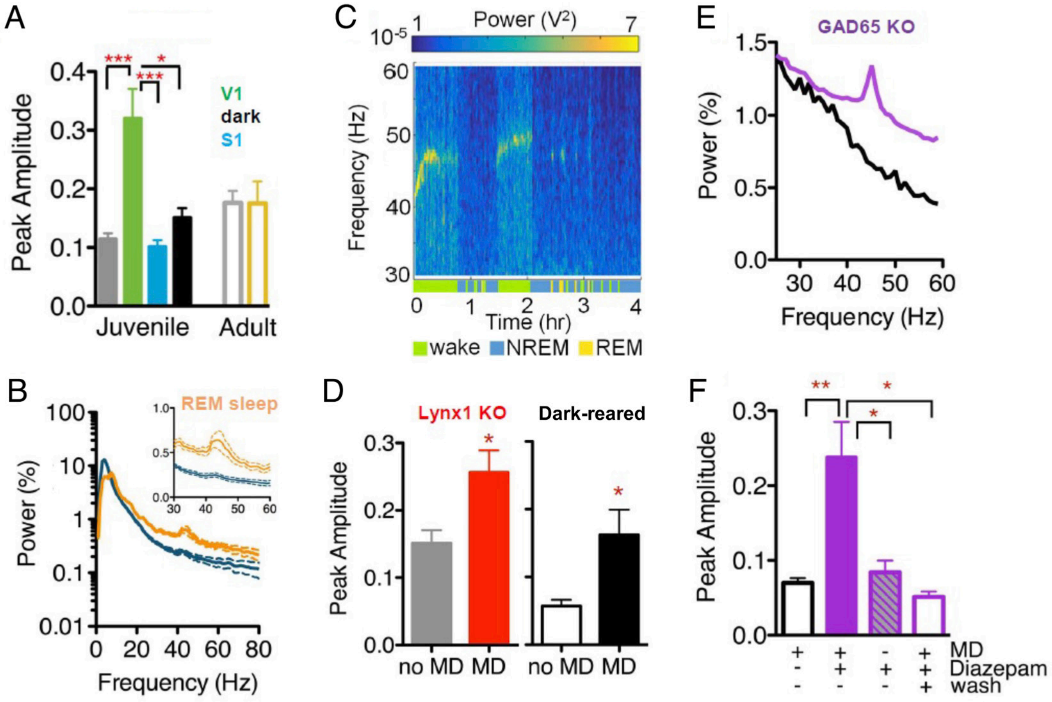

Fig. 2. γ power rise reflects level of adult plasticity. (*A*) The mean maximal γ power amplitude, comparing juvenile wt mice following MD (green, $n = 14$), no MD (gray, $n = 12$), MD with EEG over S1 (blue, $n = 9$), and MD recorded in darkness (black, $n = 10$; 1-way ANOVA with Tukey's Comparison, $*P < 0.05$, $***P < 0.001$), or adult wt mice following no MD (gray, $n = 10$) or MD (yellow, $n = 12$; Mann–Whitney test, $P = 0.1065$). (*B*) Mean NREM (blue) and REM (orange) power spectra of juvenile wt mice in the first 2 h following MD, shown as total percentage of power. Insert expands low γ band region. (*C*) EEG power spectrum from representative adult *Lynx1* KO mouse following MD, with behavioral state indicated by color bars below surf plot. (*D*) The mean maximal γ amplitude for the first hour, normalized to NREM γ power, error bars show SEM (*t* test, $*P < 0.05$). *Left* panel shows adult $Lynx1^{-/-}$ mice following MD (red, $n = 10$) or no MD (gray, $n = 8$), *Right* panel shows adult DR mice following MD (black, $n = 5$) or no MD (white, $n = 4$). (*E*) Power for the first 2 h of recording comparing representative juvenile $GAD65^{-/-}$ mice following MD treated with either saline (black) or diazepam (purple). (*F*) Mean maximal γ power amplitude in $GAD65^{-/-}$ juvenile mice with saline treatment and MD (black, no-fill, $n = 11$), with diazepam treatment and MD (juvenile and adult ages combined, purple, $n = 15$), with diazepam treatment and no MD (purple, striped, $n = 9$) and with diazepam treatment as juveniles and MD as adults (wash, purple, no-fill, $n = 5$). one-way ANOVA with Tukey's Multiple Comparison, $*P < 0.05$, $**P < 0.01$.

Previous reports have found that deprivation-induced shifts in PV-cell activity are state dependent (11, 24). Cortical activity patterns vary across brain states, differing most dramatically between "sleep" and wakefulness. As expected, baseline γ-power dropped during NREM sleep and the deprivation-induced γ-signature disappeared (blue segments; Fig. 1*B*). Notably, the peak in γ-power reappeared during REM sleep bouts (orange segments; Figs. 1*B* and 2*B*). State differences in acetylcholine drive slow versus fast oscillatory patterns typically observed in different behavioral states (25). Reactivation of the γ-power peak in REM sleep suggested cholinergic signaling may be involved. To explore this hypothesis, we tested mice lacking Lynx1, an endogenous prototoxin that normally dampens cortical nicotinic acetylcholine receptor signaling in adulthood (26). In comparison with nondeprived mice, MD yielded a significant rise in γ-power in adult $Lynx1^{-/-}$ animals (mean maximum γ-power no MD = 0.151 ± 0.019, 8 mice; MD = 0.256 ± 0.033, 10 mice; Fig. 2 *C* and *D* and *SI Appendix*, Fig. S2*A*). As in the young WT mice, this γ-power rise was state dependent and reactivated during REM sleep (orange segments; Fig. 2*C*).

Rapid γ-Signature Is Robustly Associated with CP State. Both the absence of MD-induced γ-power in adult WT mice and its presence in adult $Lynx1^{-/-}$ animals, which display extended sensory CPs (27, 28), suggest that rapid cortical plastic events are an indicator of open CP state. Therefore, we systematically investigated this relationship across other conditions that shift developmental timing. First, rearing pups in total darkness (DR) from birth delays both the maturation of inhibitory circuits in V1 and CP onset (29). We exposed adult DR mice to light for one day in order to trigger the opening of the CP for ocular dominance. Following MD, these adult mice exhibited a significant rise in γ-power when compared with unsutured DR mice (mean maximum γ-power no MD = 0.057 ± 0.010, 4 mice; MD = 0.162 ± 0.037, 5 mice; Fig. 2*D* and *SI Appendix*, Fig. S2*B*).

Failure to open the CP in DR mice is due to immature cortical inhibition (30), which may also be inadequate to support γ-power. To directly address this hypothesis, we tested mice lacking GAD65. These animals have constitutively low levels of evoked GABA release preventing CP opening, which can be rescued by boosting GABA function at any age (13). MD failed to induce a γ-peak even in young animals (Fig. 2*E* and *SI Appendix*, Fig. S2*C*). However, diazepam treatment for 3 d restored the MD γ-peak over V1 in $GAD65^{-/-}$ mice regardless of age (*SI Appendix*, Fig. S2*D*). Diazepam treatment alone without MD did not trigger a rise in γ-power (mean maximum γ-power, saline + MD = 0.074 ± 0.024, 11 mice; diazepam + MD = 0.238 ± 0.0.47, 15 mice; diazepam no MD = 0.084 ± 0.044, 9 mice; Fig. 2*F*). In turn, once a CP was induced by prior diazepam treatment as juveniles then allowed to close (13), MD in adult $GAD65^{-/-}$ mice no longer induced a peak in γ-power (mean maximum γ-power = 0.052 ± 0.016, 5 mice; Fig. 2*F*, hollow purple bar).

Rapid TC Synapse Loss onto PV-Cells Heralds CP Plasticity. To examine the synaptic response to this rapid change in oscillatory activity in V1, we optimized a brain slice preparation preserving the TC projection from Lateral Geniculate Nucleus (LGN) to binocular V1 (22). An oblique slice angle was optimized by age to capture the circuitous fiber trajectory of TC axons both before (P16-18) and during (P24-27) the classical CP (Fig. 3*A*). Connectivity was confirmed by voltage-sensitive dye imaging in response to electrical stimulation of the LGN (Fig. 3*B*). Anatomical boundaries within V1 were established by light exposure to the ipsilateral eye prior to TC slice preparation of Fos-GFP mice: binocular V1 extended laterally (~0.5 mm) from the narrowing white matter tract and contained significantly more cells activated by input from the ipsilateral eye than in neighboring monocular V1 or V2 (Fig. 3*C*). Finally, separate tracer injection into the right and left eyes defined the contralateral and ipsilateral regions within the LGN (Fig. 3 *D*, *Right*). Minimal stimulus currents applied through a pipette placed onto the ipsilateral LGN patch to elicit a V1 response were significantly lower than those for fibers exiting the LGN (Fig. 3 *D*, *Left*), reflecting lower somatic vs. axonal action potential threshold (31, 32).

Minimal stimulus current-evoked TC input drove sharp AMPA-mediated excitatory postsynaptic currents (EPSCs) in layer IV cells of binocular V1 already before the CP (Fig. 4 *A* and *B*). Onset delay (< 9 ms) and jitter (< 0.5 ms) in both PV-GFP and non-PV cells indicated a monosynaptic response (Fig. 4*C*). Notably, EPSC size onto PV-cells was stronger, faster and more precise than that onto neighboring pyramidal cells, as also observed for TC input bias in somatosensory and auditory cortices (28, 33). Threefold larger single-fiber EPSCs were accompanied by a lower paired pulse ratio (PPR), indicating a higher TC release probability onto PV-cells than onto non-PV cells (Figs. 4 *A* and *B* and 5*A*). The shorter onset and faster decay kinetics in PV-cells (Fig. 4*C*) was further consistent with their differential expression of AMPA receptor subunits (34). Importantly, synapse strength and release probability were already fully mature before CP onset (P16-18) similar to the peak of the CP (P24-27), indicating that the TC-to-PV synapse is already stable over this developmental transition (Fig. 4*B*).

We then probed TC connection strength following MD under various conditions. Strikingly, EPSC amplitude onto PV-cells was reduced by nearly half as early as 2 h after MD (Fig. 4*D*). Unlike the transient γ-peak, TC-EPSCs onto PV-cells remained weak through 3 to 4 d of MD (Fig. 4*E*; short-term MD), at which point TC synapse structure (4), dendritic spines (5), and visual response (8) are fully impacted. Consistent with a presynaptic locus, the PPR onto PV-cells was nearly doubled by short-term MD (Fig. 5 *A* and *B*). In the presence of TTX, miniature EPSC (mEPSC) revealed a large decrease in both frequency and amplitude of events onto PV-cells after short-term MD. Surprisingly, TC input onto nearby pyramidal cells was unaltered by short-term MD (Fig. 4*E*) despite a modest decrease in mEPSC amplitude (*SI Appendix*, Fig. S3). As expected for the pivotal role of PV-cells in CP plasticity (9), this TC synapse was only altered when the animal was in a plastic state. Short-term MD neither before CP onset (P16-8) nor in $GAD65^{-/-}$ mice during the typical CP (P24-28) weakened TC-to-PV synapse strength (Fig. 4*E*).

Finally, we examined structural changes at the synaptic level. Using vGluT2 to identify TC terminals (35), we compared synaptic puncta onto PV-cell bodies in control animals and after MD (Fig. 5 *C* and *D*). After 3 d of eyelid closure, there was a significant decrease in bouton size but not number surrounding PV-cells in layer IV (Fig. 5*D*). One additional day of MD reduced their number (Fig. 5*E*), reflecting synapse elimination leaving behind only the larger boutons. Thus, the earliest plastic events following sensory deprivation in V1 start with an immediate loss of functional TC input onto PV-cells, consistent with rapid changes in EEG γ-power, followed by presynaptic TC-to-PV synapse shrinkage and pruning several days later. It is likely that these rapid TC-to-PV

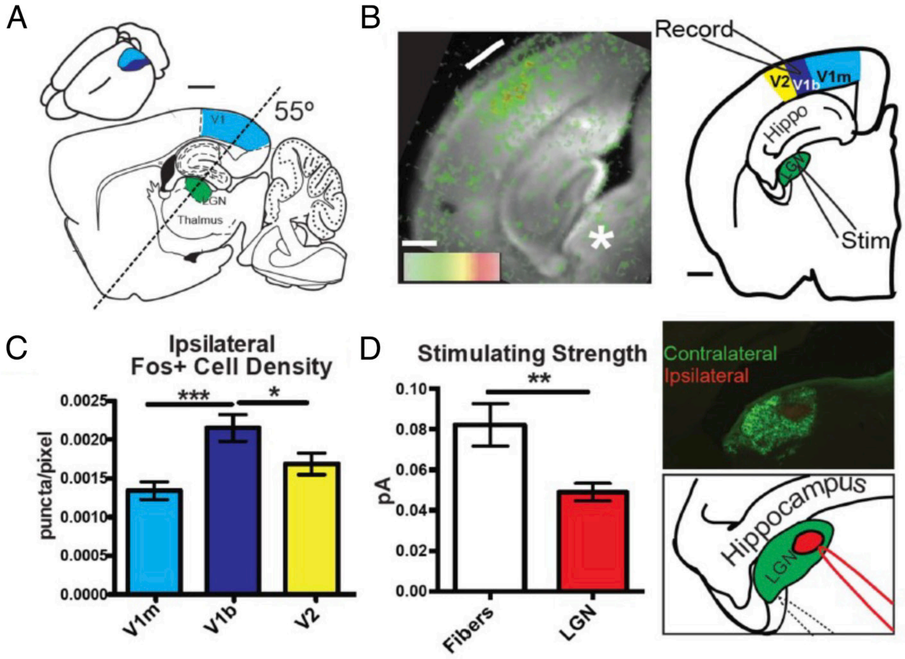

Fig. 3. Validation of the thalamocortical slice. (*A*) Diagram locating LGN and V1, approximately 2 mm lateral of midline, demonstrating the plane of TC slice (dashed line). Inset shows approximate location of monocular V1 (light blue) and binocular V1 (dark blue) in the 3D mouse brain. (Scale bar 500 μm.) (*B, Left*) Individual frame from voltage-sensitive dye recording 8 ms after electric stimulation to the LGN showing strong layer IV activation. (*B, Right*) Diagram of TC slice indicating location of stimulating electrode (Stim) in the thalamus and recording location in the binocular zone of the primary visual cortex (V1b). (Scale bar 500 μm.) (*C*) Quantification of Fos staining in the visual cortex after light stimulus to the ipsilateral eye ($n = 9$; one-way ANOVA, $*P < 0.05$, $***P < 0.001$). (*D, Upper Right*) Cholera toxin eye injections showing terminals in LGN and separation of ipsilateral and contralateral zones within the TC slice. (*D, Bottom Right*) Diagram of stimulation electrode placement in TC LGN (solid red line) or in fiber tract (dotted line). (*D, Left*) Quantification of initial experiments stimulating either fiber tract or LGN needed to elicit single fiber EPSC. Lines at ± SEM (fiber tract $n = 53$, LGN $n = 40$; $P < 0.05$, Mann–Whitney test).

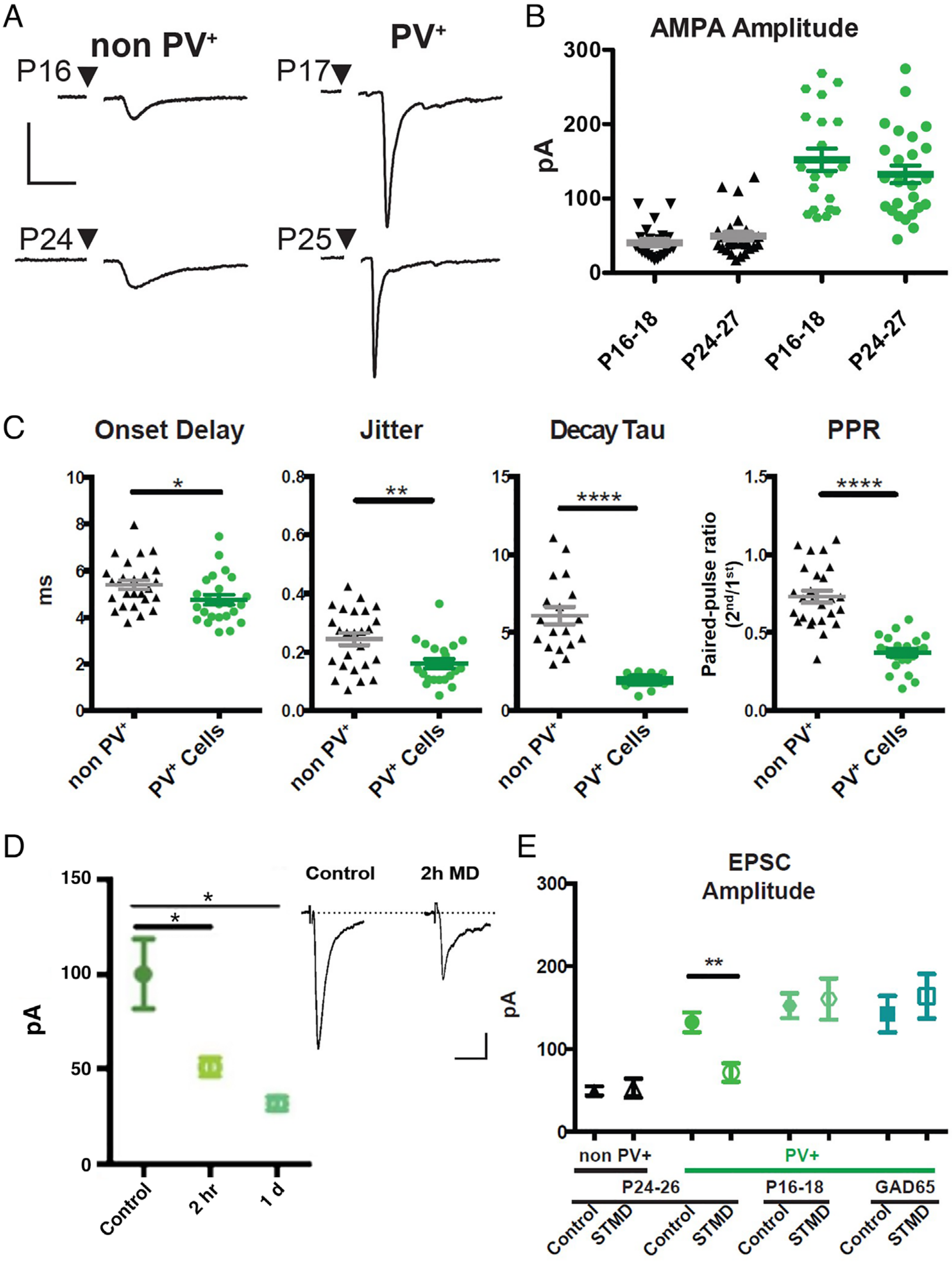

Fig. 4. Thalamocortical input onto PV cells is stronger and more plastic. (*A*) Example traces of AMPA mediated single fiber TC EPSCs onto non-PV cells and PV cells before and during the critical period. (Scale bar 50 pA, 10 ms.) (*B*) Quantification of single fiber TC inputs onto non-PV cells (black) and PV cells (green) before (P16-18) and during (P24-27) the critical period. (*C*) Thalamocortical synapse onto PV+ cells has a higher release probability as indicated by smaller paired pulse ratio, in addition to a quicker onset, less jitter, and faster decay constant than non-PV$^+$ cells. (non-PV$^+$ n = 30, PV$^+$ n = 26). (*D, Right*) Example traces of PV$^+$ cells in control and after 2 h of MD (Scale bar, 20 pA, 10 ms) (*D, Left*) 2 h and 24 h of MD equally decreases the TC input onto PV+ cells. (control *n* = 8, 2 h *n* = 20, 1 d *n* = 7). (*E*) STMD shifts TC EPSCs onto PV+ cells during the critical period but not before the critical period begins nor in animals with reduced GABA signaling (non-PV Control *n* = 30, non-PV STMD *n* = 12, PV+ Control *n* = 24, PV+ STMD *n* = 14; P16-18 Control *n* = 22. P16-18 STMD *n* = 7; GAD65 KO Control *n* = 5. GAD65 KO STMD *n* = 5). Values are mean ± SEM. one-way ANOVA *$P < 0.05$, **$P < 0.01$, ***$P < 0.001$.

events herald later ocular dominance plasticity and acuity loss as MD proceeds, as all of these events were found to be sensitive to microglial inhibitors [*SI Appendix*, Fig. S4; (36)].

Mathematical Model of Deprivation-Induced Intrinsic Interneuron Network γ-Rhythm (ING). We constructed a biophysical model of thalamic input into layer IV cortical circuits during early developmental periods (pre-CP and CP) (Fig. 6*A*). The model consists of TC-cells, cortical fast-spiking PV-cells and pyramidal cells with 40 neurons of each type. In the pre-CP, all intracortical connections are very weak (silent synapses) representing the unstructured and weak network conditions assumed to be present during early developmental periods. In the pre-CP, PV-cells are connected all-to-all via weak GABA$_A$ synapses.

We assume two populations of PV-cells: one receiving TC input relayed from the right eye and the other receiving TC input originating from the left eye (Fig. 6*A*). Each TC cell in a population connects with all PV-cells in their respective target population. Thus, each PV-cell receives 20 TC inputs. The strong topographic organization present in the early TC system (37–39), the initially sparse innervation of the cortex by the thalamus (40) and the abundance of silent synapses in early development (41) are modeled by each TC-cell connecting strongly to one pyramidal cell and one PV-cell; but otherwise, TC connections are very weak

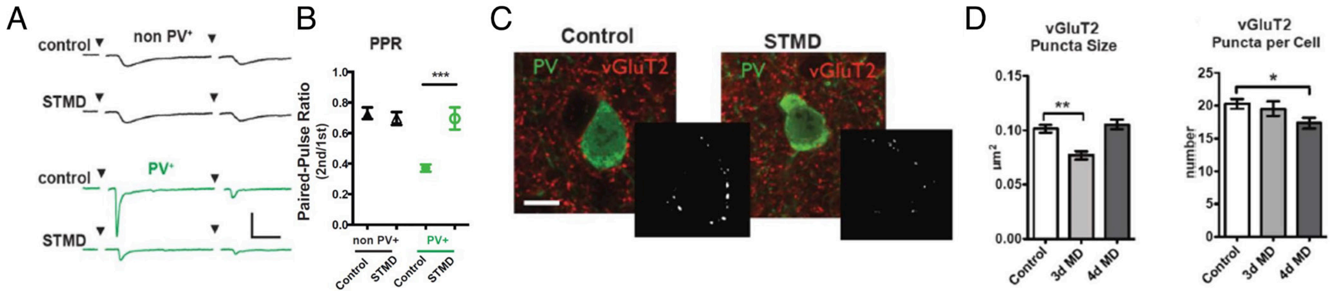

Fig. 5. Presynaptic thalamocortical changes after short-term MD. (*A*) Example traces from control mice and STMD mice of single fiber TC input onto non-PV (black) and PV+ (green) cells. (Scale bar 50 pA, 10 ms.) (*B*) Decrease in PPR suggests changes in release probability after STMD in the PV+ cell (Values are mean ± SEM. non-PV Control $n = 30$, non-PV STMD $n = 12$, PV+ Control $n = 24$, PV+ STMD $n = 14$). (*C*) PV and VGluT2 staining of PV$^+$ cells in control and MD animals after 3-d MD. *Inset* images after establishing the ROI and thresholding. (Scale bar 20 μm.) (*D*) 3 d of MD shows a decrease in puncta size while after 4 d there is a decrease in number of puncta (*E*) ($n = 4$ animals per group, 10 cells for each area per animal. one-way ANOVA with Tukey's Multiple Comparison $*P < 0.05$. $**P < 0.01$).

(silent) (Fig. 6*A*). In fact, we find that this pre-CP connection scheme is necessary to prevent plasticity during the pre-CP (see *SI Appendix* section entitled "Relaxation of model assumptions") and enables a simple and principled representation of early thalamic input to the cortex. Although, pyramidal cells receive input from the TC cells of both TC populations, since only one TC-to-PYR connection is strong enough to elicit spiking for each layer IV PYR (throughout all simulations), the TC-to-PYR connections are effectively monocular.

The transition from the pre-CP to the CP state is achieved by adding electrical connections between PV-cells and strengthening PV-to-PV inhibition, as suggested by experimental work (23, 42). At CP onset, PV-cells connect electrically with all other PV-cells of their own population (those receiving input derived from the right or left eye, respectively), and GABA$_A$ connections between all PV-cells are strengthened. Assuming there is greater competition between PV populations than within populations, GABA$_A$ conductance is stronger for inhibitory connections between versus within populations (see *SI Appendix* section entitled Relaxation of model assumptions for simulations without this assumption).

We model MD by stopping the spiking of half of the TC-cells (those receiving input from the deprived eye), which effectively stops the spiking of all PV and pyramidal cells to which those TC-cells project strongly (Fig. 6*B*). We refer to the population of PV-cells deprived of TC input as PV$_{MD}$ cells and to the population of PV-cells receiving TC input from the open eye as PVo cells (Fig. 6*A*). We model the local field potential (LFP) as the sum of inhibitory currents onto pyramidal cells (43–45) (*SI Appendix, Methods*).

MD Induces ING in the PVo Population. A finely tuned γ-oscillation around 40 Hz emerges in the model LFP immediately upon loss of input to half of the TC-cells during the CP (MD$_{early}$ condition) but fails to do so without MD (Fig. 6*C*), consistent with our experimental results (Figs. 1 *B* and *C* and 2*A*). As observed in vivo (Figs. 1*B* and 2*C*), the γ-oscillation induced by MD in the model persists for a discrete period of time, gradually increasing in frequency before finally disappearing (MD$_{late}$ condition) (Fig. 6*C*). Our computational model thus reproduces the major EEG features of the acute yet transient rise in γ-power following MD during the CP in mice.

The model further allows us to observe the spiking and network dynamics of the thalamic and cortical neurons to determine causative factors underlying the MD-induced γ-rhythm as well as network changes brought about by the γ-rhythm. MD is modeled

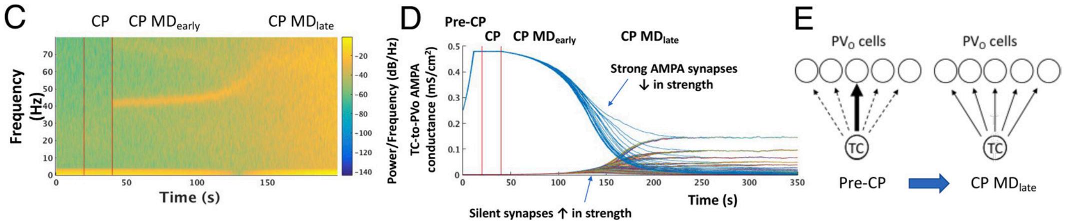

Fig. 6. Computational model of MD during the CP. (*A*) Schematic diagram of the model thalamocortical network. TC$_{MD}$/TC$_O$ refers to the TC population receiving input from the monocularly deprived and open eye, respectively. PYR$_o$ / PYR$_{MD}$ and PV$_o$ / PV$_{MD}$ refer to the populations of pyramidal or PV-cells receiving strong input from TC$_O$ and TC$_{MD}$, respectively. (*B*) Representative raster plots of all neurons in the thalamocortical network during the pre-CP, CP and CP MD$_{early}$ and CP MD$_{late}$ states. (*C*) Spectrogram of model LFP as the model transitions from pre-CP to CP (first vertical red line) then to CP+MD (second vertical red line). (*D*) Evolution of all model TC-to-PV$_O$ synaptic AMPA conductances through the pre-CP, CP and CP+MD states (red vertical lines demarcate the boundaries between states). Each curve shows the AMPA conductance of one TC-to-PV$_O$ synapse over time. (*E*) Schematic of the redistribution of TC-to-PV$_O$ connectivity induced by CP MD. Arrow thickness represents connection strength.

by stopping the spiking of half of the TC neurons (TC_{MD} neurons) as seen by lack of activity in neurons 1 to 20 in the raster plot during CP MD (Fig. 6*B*). As a consequence of loss of TC_{MD} input, both PV_{MD} neurons and pyramidal cells receiving strong input from TC_{MD} stop spiking. In contrast, the spiking of the PVo neurons, which faithfully followed strong TCo input during the pre-CP, begin to spike synchronously at intervals in the γ-frequency range following MD (Fig. 6*B*). This spontaneously formed interneuron ensemble of PVo cells is an expression of a well-characterized rhythmic dynamic in neuronal systems termed an interneuron γ (ING) rhythm (19, 20). We note that the formation of ING occurs immediately upon cessation of PV spiking from the PV_{MD} population deprived of TC input (Fig. 6 *B* and *C*).

Notably, we do not see an acute rise in γ-rhythms as the model transitions from pre-CP into the CP without MD (Fig. 6*C*), again consistent with our experimental finding (Fig. 1 *B* and *C*). This lack of an abrupt onset of γ-rhythm following CP opening alone (i.e., addition of electrical connections and strengthened inhibition between PV-cells) is consistent with known mechanisms of ING, which require sufficient interneuron excitation. The latter condition is provided by MD: release of inhibition from the deprived PV population (PV_{MD} cells) allows the PV cells receiving input from the open eye (PVo cells) sufficient excitation to form ING. Thus, the MD-induced formation of ING during the CP is due to a dramatic and sudden imbalance of excitation to the two interconnected interneuron populations, leaving the PVo population in a high excitation state and thus able to form ING.

ING Alters TC-to-PV Spike Timing and Enables Rapid Plasticity. The formation of an ING ensemble has immediate consequences regarding network plasticity. Since the spike timing of the PVo cells is no longer driven exclusively by the TC input, but additionally has its own intrinsic ensemble dynamics, spike timing between TC-cells and PVo cells is no longer solely sequentially pre–post as occurs in the pre-CP (*SI Appendix*, Fig. S5*A*). The consequence of this altered spike timing is a rapid and progressive depression of AMPA connection strength in the strong TC-to-PVo connections (Fig. 6*D* and *SI Appendix*, Fig. S5*B*). This is consistent with the finding of decreased TC-to-PV AMPA responses following MD during the CP in mice (Fig. 4 *D* and *E*). In contrast, TC-to-PV_{MD} connections remain unchanged since no spike-timing-dependent plasticity occurs in the absence of spiking (see "Synaptic Plasticity Rules" in *SI Appendix*, *Methods*). The TC input to the pyramidal cells also remains unchanged due to the unaltered spike timing between TC cells and pyramidal cells following MD (*SI Appendix*, Fig. S5 *A* and *C*), consistent with our experimental observations of TC-to-PV cell-specific plasticity (Fig. 4*E*).

In contrast, modeling MD before the CP does not yield any significant changes in oscillatory power (*SI Appendix*, Fig. S5*D*) or any plastic changes (*SI Appendix*, Fig. S5*E*): due to lack of electrical connections in the pre-CP, the ING rhythm does not emerge and pre–post spiking from TC-to-PV cells remains unaltered – again consistent with the experimental results showing lack of plasticity before the CP (Fig. 4*E*). These results point to the developmental importance of gap junctions between PV interneurons in regulating behaviorally relevant plasticity during the CP.

The rapidity of the ING-induced plastic changes occurs due to the ING-imposed ~25 ms PVo interspike interval (Fig. 6*B*, see CP MD_{early}), which ensures significant plasticity in TC-to-PVo connections (either LTD or LTP) on every γ-cycle (*SI Appendix*, Fig. S5*F*, see Synaptic Plasticity Rules section in *Methods*). This accounts for the rapid evolution of TC-to-PV plastic changes observed both in the model and in vivo. We note that plasticity in the model evolves more rapidly than in vivo (100 s of model time corresponds to approximately 2 h of in vivo time) due to the instantaneous nature of the plastic changes in the model. In contrast, in vivo plastic changes are not instantaneous but rather depend on intracellular signaling pathways as well as periods of sleep (11, 46). In a subsequent section below, we examine why LTD predominates over LTP in altering the strong TC-to-PVo synapses. Overall, our modeling suggests that the MD-induced γ-rhythm is a signature of ING, an autonomous cortical dynamic independent of specific thalamic input. The autonomous nature of ING alters TC-to-PV spike timing, resulting in an observed decrease in TC-to-PV connectivity strength.

Rising γ-Frequency and Eventual Disappearance Reflects Strengthening of Silent Synapses. Our experimental recordings show the frequency of the γ-rhythm increasing over several hours following MD before finally disappearing (Figs. 1*B* and 2*C*). The model reproduces these findings (Fig. 6*C*) and reveals that these features of the γ-frequency signature are due to increasing the strength of previously silent TC-to-PV synapses, which follow the decrease in previously strong TC-to-PV synapses (Fig. 6*D*). Decreasing the conductance of the strong TC-to-PV synapses is essential to unmask the contribution of silent TC-to-PV synapses due to a limit built into the model on the overall amount of excitation a PV-cell can receive, a principle related to homeostatic synaptic scaling of excitatory synapses (47, 48). During the pre-CP, TC-to-PV synapses with the greatest AMPA conductances dominate the overall input to any particular PV-cell, while the remainder of TC-to-PV synapses remain silent (Fig. 6*D*). Standard Hebbian plasticity rules at the TC-to-PV synapse maintain the dominance of this strong connection, not allowing the silent TC-to-PV synapses to emerge. Decreasing the strength of the strong TC-to-PV synapse in response to ING opens a window of opportunity for the silent synapses to increase in strength (Fig. 6*D*).

Both the rising γ-frequency and its eventual disappearance are signatures of TC-to-PV conductance increases in previously silent synapses. Since the overwhelming majority of TC-to-PVo synapses (19/20 synapses to each PVo cell in our model) are silent at the start of the CP, the overall effect of weakening previously strong synapses to unmask previously silent synapses is to increase excitation onto the PV-cells. In turn, as PV-cell excitation increases, the γ-frequency of the ING increases (20). Thus, our model suggests that the experimentally observed time period over which MD-induced γ-oscillations are increasing in frequency corresponds to when silent TC-to-PV synapses are becoming active. Eventually, the majority of TC-to-PV synapses gradually become similar in strength. This transforms the spiking of PV-cells from a network in which one PV-cell responds only to the input of one, strongly connected TC-cell to a network in which the total TC population guides the PV network spiking activity (Fig. 6*E* and *SI Appendix*, Fig. S6).

As this transition takes place, the finely tuned γ-rhythm fades out and is replaced by a broadband increase in power (Fig. 6*C* MD_{late}). This is due to the overall increase in TC population AMPA to the PV-cells, which drives them to spike in response to TC population activity: thus, ING is replaced by PV-cells being synchronized to TC population input, which is nonrhythmic and generally at a faster rate than ING (Fig. 6*B*, CP MDlate) and appears in the model LFP as broadband activity. Thus, our model predicts that the disappearance of narrow-band γ-rhythm after MD corresponds to the time when TC-to-PV synapses have strengthened enough to be patterned by TC population activity.

Complementary changes in TC synapse strength in response to ING reflect the nonsymmetrical spike-timing-dependent plasticity rule of PV-cells in which LTD has a longer time constant of decay than LTP (*SI Appendix*, Fig. S5*F* and *Methods*) as well as the upper and lower limits on AMPA conductance and the way Hebbian rules act around these limits. Specifically, silent synapses are close to the lower limit of AMPA conductance (near gAMPA = 0), which favors LTP as maximal LTD cannot occur if that moves gAMPA below the lower limit; while, LTP can always be maximally instantiated near the lower conductance limit. Thus, if spike-timing-dependent plasticity is allowed to occur, and pre–post spikes are randomly aligned as occurs with TC-to-PV synapses during ING, silent synapses will be strengthened. The opposite phenomenon occurs for the strong TC-to-PV synapses, which are near the upper limit of AMPA conductance favoring LTD over LTP. Once away from the upper and lower limits of AMPA conductance, synapses compete until a semistable equilibrium is reached in which all TC-to-PV synapses become more homogeneous in strength (Fig. 6*D*).

These results suggest that the temporal dynamics of the EEG γ-rhythm following MD are signatures of TC-to-PV circuit rewiring. The network evolves from a TC-to-PV network in which each PV cell is predominately driven by one strong TC input (*SI Appendix*, Figs. S5*A* and S6*A*) to a network that uses the collective TC input to drive a strong, synchronized PV output (*SI Appendix*, Fig. S5*A* and S6*B*). The PV output is both weak and narrowly defined in scope during the pre-CP: one PV-cell responds primarily to one TC-cell spike. In contrast, after CP rewiring the PV output is strong (an ensemble of PV-cells transmits synchronously) (*SI Appendix*, Fig. S6*C*) and broader in scope (PV-cells respond to many combinations of TC input) (*SI Appendix*, Fig. S6*B*).

The CP rewiring after MD also improves sensitivity of PV-cells to TC input: namely, input that previously would not have caused PV-cell spiking now reliably produces robust PV-cell output (*SI Appendix*, Fig. S6 *A* and *B*). Gap junctions between PV-cells underlie their increased sensitivity to TC input since electrical coupling between cells increases their excitation and effectively lowers their spiking threshold (23, 49). Relatively homogeneous TC-to-PV synapses, along with gap junctions, contribute to all PV-cells spiking synchronously in response to TC input, since each PV-cell is receiving approximately the same amount of depolarizing input as all others. Increased sensitivity in turn enhances the fidelity of TC transmission to the cortex by post-MD network modifications: the PV population more faithfully encodes the collective output of the TC population (*SI Appendix*, Fig. S6*B*).

Overall, our results suggest the post-MD γ-signature serves as a functional read-out of TC-to-PV connections transitioning from a network producing weak feedforward inhibition from single TC-cells to a network that sensitively responds to TC population statistics, amplifying this signal, and thus sending coordinated and powerful inhibition within cortical circuits.

Compensatory Mechanisms Limit the Rise in Broadband γ-Power. Some form of homeostatic renormalization of E-I balance is likely to take place after the restructuring of TC-to-PV synapses, as overall excitation to PV-cells has grown considerably over the course of MD (*SI Appendix*, Fig. S6*C*). Common mechanisms for decreasing PV excitability include a compensatory, uniform decrease in all TC-to-PV synapses, decreased PV-to-PV electrical connectivity, increased PV-to-PV GABAergic inhibition or regulation of specific intrinsic PV membrane currents leading to additional membrane hyperpolarization (e.g., increasing Cl^- leak).

To examine the effect of decreasing PV excitability, we lowered the maximal gap junctional conductance between PV-cells after bouts of simulated sleep (simulated by reducing cortical spiking), hypothesizing that repeated activity bursts during slow-wave sleep may decrease coupling between PV cells as they do between cells in the thalamic reticular nucleus (50). These simulations reproduced the slight drops in γ-frequency after bouts of non-REM sleep seen in our mouse experiments (Fig. 1*B*) and mitigated the degree of broadband LFP activity at MD_{late} stages (Fig. 7*A*). Yet, the decrease in PV-cell activity did not affect the overall progression of TC-to-PVo synapses toward homogeneity (Fig. 7*B*), regardless of a lack of plasticity during sleep due to the absence of spiking. Toward the end of the simulation, the almost perfect synchrony between PV-cells which occurs when gap junctions remain strong (Fig. 6*B*) was replaced by a jittered synchrony when gap junctions were weakened (Fig. 7*C*), which ultimately decreases broadband γ-power (Fig. 7*A*), as observed in vivo (Fig. 1*B*). As such, we expect that some sort of compensatory mechanism for PV overexcitability accounts for these changes in vivo.

Competitive ING Dynamics Arise between PV Populations During Normal CP Experience. Modeling the CP without MD elicits a slow onset of ING-like dynamics in both populations of PV cells expressed at alternate times (*SI Appendix*, Fig. S7*A*). The CP is modeled by adding gap junctions between a population of PV-cells and increasing the $GABA_A$ conductance between PV neurons. Without MD, the TC inputs from the two thalamic regions are approximately equal (same mean spiking rate) and there is no immediate emergence of γ-activity in our model LFP (*SI Appendix*, Fig. S7*B*), rather γ-activity slowly builds up over

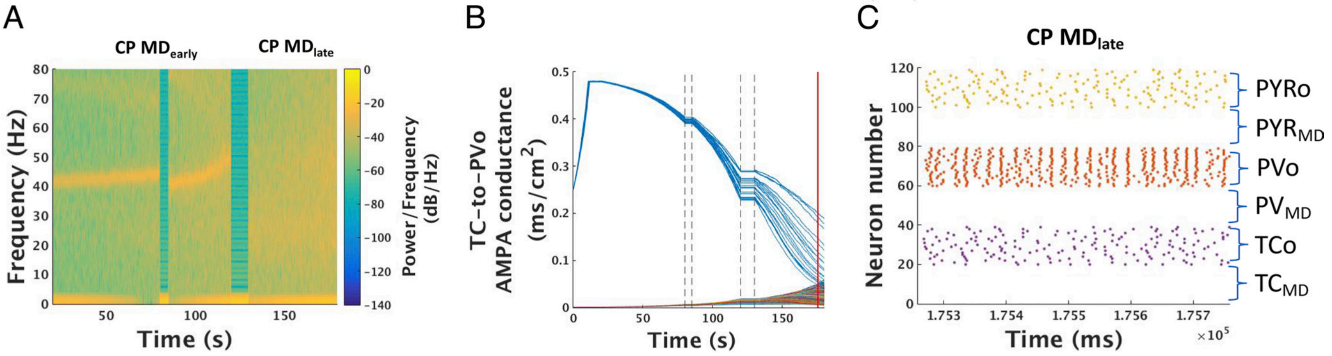

Fig. 7. Network dynamics of CP+MD with homeostasis. (*A*) Spectrogram of model LFP during the CP+MD state with interspersed periods of artificially simulated sleep (see *SI Appendix*, *Methods*) at 80 to 85 s and 120 to 130 s. Gap junction conductance was lowered after each period of sleep in order to compensate for PV-cell overexcitability. (*B*) Evolution of all model TC-to-PV_O synaptic AMPA conductances during the pre-CP (0 - 20 s) as well as during the same time period as shown in (*A*). Dashed vertical lines demarcate periods of sleep. (*C*) Raster plot of all model neurons as TC-to-PV_O synaptic conductances approach a more homogeneous state during CP MD_{late} at the timepoint indicated by the red vertical line in (*B*).

the course of the CP. Early in the CP, PV-cells largely spike in response to the strong TC input, while only occasionally spiking without it (*SI Appendix*, Fig. S5*A*). Moreover, when spiking independently of TC input, the PV spiking is coordinated with that of others such that synchronous spiking occurs among many of the PV-cells in the population (*SI Appendix*, Fig. S5*A*). This may occur as a single bout or as several bouts of synchrony occurring at γ-frequency (SI Appendix, Figs. S5*A* and S7*A*). This PV-cell dynamic is a manifestation of ING, although the ING is not as persistent or robust as in the case when MD occurs during the CP (Fig. 6*B*). ING occurs transiently in a population of PV-cells due to fluctuations in excitability: if one PV population receives more TC excitation and/or less PV inhibition from the other PV group, the more excited PV-cells can form ING.

Thus, our model suggests that ING expression during normal CP experience is sporadic and brief, resulting from competition between PV-cell populations. Each bout of ING has the potential to rewire the TC-to-PV synapses in a similar manner to the rewiring that occurs during MD. The rewiring process is longer for normal CP experience than with MD due to the noncontinuous, short bouts of ING (compare Fig. 6 *C* and *D* and *SI Appendix*, Fig. S5 *B* for CP with MD and *SI Appendix*, Fig. S7 *B* and *C* for CP without MD). Eventually, TC-to-PV synaptic connections even without MD lead to a γ-oscillation that increases in power and frequency (*SI Appendix*, Fig. S7*B*). This result is consistent with the gradual emergence of γ-power through the CP (21). When the silent TC-to-PV synapses have strengthened sufficiently to control the spiking dynamics of the PV population to which it connects, the ING disappears and a broadband γ-power emerges (*SI Appendix*, Fig. S7*B*).

Thus, we find that the network dynamics that evolve as they naturally pass through the CP are similar to those that evolve with MD, though not as abrupt nor necessarily restricted to one population of PV-cells. The statistics of the environment determine the outcome of the competition between groups: the PV population that receives more TC excitation undergoes more bouts of ING and thus faster TC-to-PV re-wiring, and significantly imbalanced input can lead to inhibition of TC-to-PV rewiring in the population receiving less input. These dynamics thus represent a natural coding mechanism for wiring of TC circuits based on the statistics of the environment.

Discussion

A canonical model of critical period plasticity is the gradual loss of connectivity and visual acuity through an eye deprived of vision early in life (8). Our experimental results here reveal that the initial plastic processes occur at thalamic synapses onto inhibitory PV-cells in cortical layer IV. Within hours of MD, TC input onto PV-cells drops dramatically but only when the CP is open. An immediate rise in narrowband γ-oscillations upon eyelid closure appears to drive this change in TC-to-PV synaptic strength. The fleeting γ-rhythm increases in frequency and eventually fades out over several hours, while the decrease in TC-to-PV presynaptic input persists by anatomical pruning over several days (when visual acuity is finally impacted). Computational modeling of these biological events offers a functional relationship between the initial γ-oscillation and resultant plastic changes at TC-to-PV synapses, reinforcing the pivotal role of inhibitory networks as triggers of the developmental CP (9).

Our model reproduces the emergence and evolution of the γ-oscillation after MD and suggests CP physiology is primed for the establishment of ING (interneuron γ) dynamics between cortical PV-cells. The expression of transient γ-rhythms requires sensory input, as evidenced by their absence in total darkness (Figs. 1*D* and 2*A*). ING results from elevated PV-cell excitation, with MD being an extreme form of PV cell excitation due to imbalanced thalamic input. As an autonomous cortical dynamic, ING dissociates TC and PV spiking, which leads to weakening of initially strong TC-to-PV synapses by standard STDP rules. This in turn allows previously silent TC-to-PV synapses to strengthen in our model. Molecular homeostatic factors, such as NARP (48) and SynCAM1 (51), may regulate this maturation of TC input onto PV-cells in V1. Interestingly, the upward drift of γ-oscillation frequency is a signature of the emergent boosting of silent synapses. Fade-out of the rhythm occurs once the population TC-to-PV synaptic strength has increased sufficiently to override ING dynamics.

Our model predicts that ING is the forerunner to synaptic changes at TC-to-PV circuits and as such if ING does not appear, neither will the synaptic changes. Before the CP, inhibition between PV-cells is immature (42) as are their electrical connections (23)—inadequate network conditions for ING to form. Well-developed PV-to-PV synapses enable competing PV groups to sensitively detect imbalances in thalamic input. The PV population that receives more excitation relative to its competing PV population reliably forms ING, rendering itself susceptible to TC-to-PV synaptic weight changes. Conversely, the well-known condensation of perineuronal nets (PNNs) around mature PV-cells at CP closure sufficiently diminishes their response to glutamatergic transmission, and thus their overall excitability (52), so that ING can no longer form. In fact, PNN removal by chondroitinase ABC-treatment unmasks a rapid rise in narrowband, ING-like γ-oscillation following MD in adult rats (53), supporting CP reopening. Thus, MD-induced ING is a specific PV network dynamic reflecting conditions that underlie the plastic state.

Interestingly, our simulations indicate that TC to PV circuit reorganization is largely complete with the emergence of broadband γ power in the LFP, a sign that ING has been replaced by PV neurons responding more readily to population-level TC input. Consistent with this, Faini et al. (52) found that dissolution of PNNs leads to a slow broadband increase in baseline and visually evoked γ-power 2 to 3 d later. They additionally found increased TC input to layer IV PV-cells after PNN dissolution, consistent with our model prediction of increasing TC-to-PV synaptic strength during juvenile CPs of development. However, unlike the juvenile state in which the majority of TC-to-PV synapses are initially silent, TC-to-PV synaptic strength should be more homogeneous in the adult. Thus, the rise in TC-to-PV synaptic strength is more detectable during a reopened adult CP state, once physiological conditions necessary for ING formation are reestablished.

Our study clarifies the earliest sequence of changes in V1 following MD. How the rapid TC-to-PV plastic changes in layer IV within 2 h of deprivation contribute to later changes across cortical layers is of interest. We find PV-cell activity in layer IV increases after MD specifically among those PV cells receiving input from the open eye. Considering that these interneurons connect to layer II/III interneurons (54), supra-granular PV-cell response to the open eye is expected to decrease at first and continue to evolve days after MD (10). In fact, changes in layer II/III PV-cells are detectable after 6 h of MD also in kittens (11) and initially shift their responsiveness in favor of the closed eye (10). Note that calcium imaging in mice had previously suggested that other GABA cells likely shift their responsiveness only days later (55).

Strikingly, the first recorded change in layer II/III following MD is increased coincident spiking (±10 ms) among open eye-responsive pyramidal-PV cell pairs (11). This alteration in spike timing takes place 1 h after MD, exactly when we found MD-induced γ-rhythms to emerge. An increase in nearly coincident spike timing between pyramidal-PV cell pairs is precisely what would be expected from layer IV ING that synchronously releases them from inhibition for only a very short period of time at the end of each γ-cycle (19, 20). Such an increase in nearly coincident spiking between pyramidal-PV cell pairs is also expected when mesencephalic stimulation successfully drives γ-rhythms in adult cat V1 to enable plasticity of receptive field properties (56).

Shifts in neuromodulatory activity over the first several hours of MD may contribute to the transient nature of the observed rise in γ-power. The presence of a γ-peak in both wake and desynchronized (REM) sleep, but not in NREM sleep, suggests cholinergic signaling may be involved. Visual γ-power can be dramatically increased for several hours by pairing visual stimuli even briefly with cholinergic agonists (57). A similar ‘novelty’ detection may arise post-MD, with concordant loss of thalamic drive onto PV-cells and increased cholinergic tone creating a cortical state that favors γ-activity. Acetylcholine has long been appreciated to play an important role in regulating CP plasticity (58). During the auditory CP, acetylcholine activates layer I inhibitory interneurons, which in turn inhibit PV-cells from the top down (28). Boosting cholinergic signaling in adult mice either pharmacologically or through genetic deletion of *Lynx1* re-opens CP plasticity across brain regions (27, 28).

One theory of CP timing postulates that inhibition opens windows of plasticity by increasing the signal-to-noise ratio (59), shifting the brain’s sensitivity to external stimuli as opposed to internally generated activity. By locally altering signal-to-noise dynamics of a network (60), the γ-rhythm may mediate shifts between external and internal cues. Our modeling supports the notion that a function of the rewired TC-to-PV network in the adult cortex may relate to suppression of noise as a means of increasing fidelity of TC signal transmission when passing sensory input to the cortex. Whereas TC-to-pyramidal cell synapses likely encode the specificity of the input, TC-to-PV connections responding to the population TC input provide background inhibition. This filters out the weaker pyramidal cell activity unrelated to the specific TC input. Our study suggests CP rewiring of TC-to-PV input contributes to the ability to reduce noise, and thus increase gain, in adult circuits.

We also provide an explanation of how more subtle naturalistic experiences early in life can ultimately shape neural circuits during the CP. While a strong, transient γ signature (lasting ~110 s of simulation time) follows strong input imbalance (like MD) in the model, only brief ING (~10s of milliseconds) follows the less dramatic fluctuating thalamic input statistics under normal environmental conditions. Small plastic changes then accrue such that TC-to-PV plastic changes occur predominately in the TC pathways receiving environmentally dominant stimuli. Overall, the EEG γ-signature following MD is a read-out of TC-to-PV connections transitioning from a network that provides weak feedforward inhibition of strong thalamic signals to a network that sensitively responds to TC population input and amplifies this signal, providing coordinated and strong inhibition to local cortical areas.

More broadly, γ-oscillations are associated with cognition and altered in cognitive disorders like autism and schizophrenia (61). Our findings now refine a potential role for these oscillations to specific time windows that enable network plasticity. Our model suggests that the physiological changes supporting ING are necessary for CP opening. Notably, adult rhythms measured once this initial plastic period has passed may fail to detect any consistent relationship to the deficits. For example, inhibiting mediodorsal and midline thalamus in mice during adolescence leads to long-lasting decreased thalamo–prefrontal projection density and later cognitive deficits (62). While γ-rhythms are not altered during task performance in adulthood, their role during the adolescent CP itself remains to be tested. In multimodal, higher order brain regions such as the prefrontal cortex, sequentially disrupted or misaligned CPs from lower order areas may further accumulate (63, 64). Appreciating how γ-oscillations contribute to developmental trajectories of plasticity offers a biomarker for tracking and treating these complex cognitive disorders.

Materials and Methods

Experimental.

Mice. C57Bl/6J, PV-GFP, *GAD65*$^{-/-}$ and *Lynx1*$^{-/-}$ mice were bred in-house and maintained on a 12-h light/dark cycle, with the exception of dark-reared animals. All experimental procedures followed Institutional Animal Care and Use Committee guidelines.

Surgery. For MD, mice were sedated with isoflurane and one eyelid trimmed and sutured shut as previously described (5). For EEG, insulated stainless steel recording electrodes (100 μm diameter, 1 mm exposed tip) were slipped between the skull and cortex with the tip overlying binocular V1 (or S1 as control) and cemented to the skull in a plug at least 4 d prior to MD. EEG recording in a sound-proof box was begun 10 min following recovery from anesthesia for MD. Recordings were high-pass filtered through a preamplifier (Pinnacle Technology 8202-SL), further amplified (Brownlee) and collected using either VitalRecorder (Kissei) or Sirenia Acquisition (Pinnacle Technology).

Slice electrophysiology. Brains were rapidly removed from deeply anesthetized mice into ice-cold choline-based cutting solution and cut at an oblique angle (~55° depending on age) to preserve TC projections to V1, as described previously (22). Slices were incubated in oxygenated ACSF (125 mM NaCl, 25 mM glucose, 25 mM NaHCO3, 2.5 mM KCl, 2 mM CaCl2, 1.25 mM NaH2PO4 and 1 mM MgCl2 (310 to 320 mOsm) for recording at 20 to 22 °C. Projections to V1 were initially confirmed by voltage-sensitive dye imaging (VSDI; 5 μg/mL Di-4-ANEPPS; Invitrogen) using a band-pass-filtered (515 and 535 nm) 150-W halogen lamp on an upright macroscope (Olympus MVX10) mounted with a high-speed CMOS-based camera (MiCam Ultima).

Single cells in binocular V1 were visualized and recorded under infrared-Nomarski DIC optics on an upright microscope (40×; Eclipse FN1, Nikon) using whole-cell patch-clamp techniques. Electrodes (2 to 4 MΩ) were filled with internal solution containing (in mM) 120 Cs-methanesulfonate, 6 CsCl, 2 MgCl2, 0.05 CaCl2, 20 HEPES, 0.02 EGTA, 10 phosphocreatine di(Na) salt, 4 Mg-ATP, 0.4 Na3-GTP, 0.15% biocytin, and 1 lidocaine derivative QX-314 (pH 7.2 with CsOH, 290 to 300 mOsm). Access resistances were maintained < 25 MΩ throughout the experiments. Bipolar glass stimulating electrodes filled with ACSF were placed in the LGN or fiber bundle to stimulate TC input with minimal current in the presence of 10 μM bicuculline.

Immunohistochemistry. Mice were perfused transcardially with paraformaldehyde (4% PFA) and brains removed, postfixed in PFA (1.5 h) and cryoprotected (30% sucrose) before slicing into coronal sections (40 μm) on a cryostat or freezing microtome (Leica). Every fourth section was collected, washed in phosphate-buffered saline (PBS), incubated in blocking solution (0.8% Triton X- 100, 20% BSA in PBS; overnight, 4 °C), then primary antibody (rabbit anti-GFP 1:2,000 (Abcam), rabbit anti-PV 1:1,000 (Swant), guinea pig anti-VGluT2 1:500 (Synaptic Systems) followed by secondary antibody (goat anti-rabbit IgG Alexa 488, goat anti-rabbit IgG Alexa 596, goat anti-guinea pig 564, goat anti mouse 488 or 633 (Invitrogen), diluted at 1:1,000 in PBS-Triton-BSA). PV-cells were imaged on a scanning confocal microscope (Olympus Fluoview FV1000TM) at 100×. The number of VGluT2 immunoreactive puncta surrounding a PV+ cell body was estimated using a custom MatLab script to identify a 1.25-μm ring around each cell. The red VGluT2 channel was thresholded to the median intensity plus 4× the SD, and all puncta within the ring, larger than 3 pixels (0.123 μm), were automatically counted and analyzed.

Computational Methods.

Neurons. Our cortico-thalamic model consists of 120 single compartment neurons with Hodgkin–Huxley-type dynamics for the intrinsic and synaptic currents. The model of cortical layer IV of V1 consists of 40 fast-spiking PV cells and 40 pyramidal cells (PYR cells). Each neuron has spiking currents (fast sodium, fast potassium and leak currents). Model pyramidal cells have an additional M-current to account for the spike-frequency adaptation observed in these cells. The model neurons were derived from (65, 66). Our thalamic model consists of 40 thalamocortical cells (TC cells) and is used solely for the purpose of passing sensory input to the cortex. Thus, TC cells are modeled using only the spiking currents. The TC cells receive independent noisy inputs to mimic fluctuating sensory inputs. Details of the equations and parameters used for each type of model neuron can be found in the *SI Appendix*, *Methods*.

Networks. Twenty TC cells receive input that is considered to come from the right eye ($\mathrm{TC_R}$) and the other twenty TC cells receive input considered to come from the left eye ($\mathrm{TC_L}$). Thalamic neurons project more strongly to one PYR cell and one PV cell and relatively weakly to all other pyramidal cells and to PV cells of the same PV population (PV cells receive input from either $\mathrm{TC_L}$ or $\mathrm{TC_R}$). PV cells that receive input from $\mathrm{TC_R}$ connect less strongly to other PV cells that receive input from $\mathrm{TC_R}$ and more strongly to PV cells that receive input from $\mathrm{TC_L}$ and vice versa for PV cells that receive input from $\mathrm{TC_L}$. This network connectivity scheme is used to model lateral inhibition between different functional units of interneurons. Additionally, gap junctions (when present) are only put between PV cells of the same functional unit (i.e., those receiving input from $\mathrm{TC_R}$ or from $\mathrm{TC_L}$).

In the pre-CP, all intracortical connections are weak because we are interested in the early (unspecified) state of the cortex. All inhibitory synapses use $\mathrm{GABA_A}$ receptor kinetics and all excitatory synapses use AMPA receptors. Cortical PV cells are connected all-to-all via $\mathrm{GABA_A}$ receptors with stronger connections between PV populations than within a population. The critical period is modeled by strengthening all PV-to-PV maximal conductances and adding electrical connections between PV neurons of the same population. Details of the equations and parameters used for the synaptic conductances are in *SI Appendix*.

Detailed methods can be found in *SI Appendix*.

Data, Materials, and Software Availability. Computer simulation data have been deposited in GitHub (https://github.com/mmccart/Quast-et-al-C--code) (67). All study data are included in the article and/or *SI Appendix*.

ACKNOWLEDGMENTS. We thank M. Nakamura, M. Marcotrigiano, E. Centofante, H. Bond for mouse maintenance; H Monyer (Heidelberg) and A Barth (Carnegie Mellon) for original PV-GFP and Fos-GFP breeders, respectively and M. Fagiolini for advice and support. Funded by NSF GRFP (DGE0946799, DGE1144152 to R.K.R), NIH Research Training Program in Sleep, Circadian & Respiratory Neurobiology (5T32HL007901-23 to R.K.R.) and NIMH Silvio Conte Center (1P0MH094271 to N.K. & T.K.H.). This article is dedicated to the memory of Prof. Miles Whittington (d.10/25/2021).

Author affiliations: [a]Department of Molecular Cellular Biology, Center for Brain Science, Harvard University, Cambridge, MA 02138; [b]FM Kirby Neurobiology Center, Boston Children's Hospital, Harvard Medical School, Boston, MA 02115; [c]Department of Mathematics, Boston University, Boston, MA 02215; and [d]International Research Center for Neurointelligence, University of Tokyo Institutes for Advanced Study, Bunkyo-ku, Tokyo 113, Japan

1. D. H. Hubel *et al.*, Plasticity of ocular dominance columns in monkey striate cortex. *Philos. Trans. R. Soci. Lond. B Biol. Sci.* **278**, 377–409 (1977).
2. A. Antonini, M. Fagiolini, M. P. Stryker, Anatomical correlates of functional plasticity in mouse visual cortex. *J. Neurosci.* **19**, 4388–4406 (1999).
3. M. A. Silver, M. P. Stryker, Synaptic density in geniculocortical afferents remains constant after monocular deprivation in the cat. *J. Neurosci.* **19**, 10829–10842 (1999).
4. J. E. Coleman *et al.*, Rapid structural remodeling of thalamocortical synapses parallels experience-dependent functional plasticity in mouse primary visual cortex. *J. Neurosci.* **30**, 9670–9682 (2010).
5. N. Mataga, Y. Mizuguchi, T. K. Hensch, Experience-dependent pruning of dendritic spines in visual cortex by tissue plasminogen activator. *Neuron* **44**, 1031–1041 (2004).
6. S. Oray, A. Majewska, M. Sur, Dendritic spine dynamics are regulated by monocular deprivation and extracellular matrix degradation. *Neuron* **44**, 1021–1030 (2004).
7. C. J. Shatz, M. P. Stryker, Ocular dominance in layer IV of the cat's visual cortex and the effects of monocular deprivation. *J. Physiol.* **281**, 267–283 (1978).
8. J. A. Gordon, M. P. Stryker, Experience-dependent plasticity of binocular responses in the primary visual cortex of the mouse. *J. Neurosci.* **16**, 3274–3286 (1996).
9. A. E. Takesian, T. K. Hensch, Balancing plasticity/stability across brain development. *Prog. Brain Res.* **207**, 3–34 (2013).
10. Y. Yazaki-Sugiyama *et al.*, Bidirectional plasticity in fast-spiking GABA circuits by visual experience. *Nature* **462**, 218–221 (2009).
11. S. J. Aton *et al.*, Visual experience and subsequent sleep induce sequential plastic changes in putative inhibitory and excitatory cortical neurons. *Proc. Natl. Acad. Sci. U.S.A.* **110**, 3101–3106 (2013).
12. S. J. Kuhlman *et al.*, A disinhibitory microcircuit initiates critical-period plasticity in the visual cortex. *Nature* **501**, 543–546 (2013).
13. T. K. Hensch, M. Fagiolini, Inhibitory threshold for critical-period activation in primary visual cortex. *Nature* **404**, 183–186 (2000).
14. M. Fagiolini *et al.*, Specific GABAA circuits for visual cortical plasticity. *Science* **303**, 1681–1683 (2004).
15. Z. J. Huang *et al.*, BDNF regulates the maturation of inhibition and the critical period of plasticity in mouse visual cortex. *Cell* **98**, 739–755 (1999).
16. U. Rutishauser *et al.*, Activity-dependent PSA expression regulates inhibitory maturation and onset of critical period plasticity. *Nat. Neurosci.* **10**, 1569–1577 (2007).
17. S. Sugiyama *et al.*, Experience-dependent transfer of otx2 homeoprotein into the visual cortex activates postnatal plasticity. *Cell* **134**, 508–520 (2008).
18. Y. Kobayashi, Z. Ye, Takao K. Hensch, Clock genes control cortical critical period timing. *Neuron* **86**, 264–275 (2015).
19. P. Jonas, M. Bartos, I. Vida, Synaptic mechanisms of synchronized gamma oscillations in inhibitory interneuron networks. *Nat. Rev. Neurosci.* **8**, 45–56 (2007).
20. M. A. Whittington *et al.*, Inhibition-based rhythms: Experimental and mathematical observations on network dynamics. *Int. J. Psychophysiol.* **38**, 315–336 (2000).
21. G. Chen *et al.*, Experience-dependent emergence of beta and gamma band oscillations in the primary visual cortex during the critical period. *Sci. Rep.* **5**, 17847–17847 (2015).
22. J. N. MacLean *et al.*, A visual thalamocortical slice. *Nat. Methods* **3**, 129–134 (2006).
23. S. Pangratz-Fuehrer, S. Hestrin, Synaptogenesis of electrical and GABAergic synapses of fast-spiking inhibitory neurons in the neocortex. *J. Neurosci.* **31**, 10767–10775 (2011).
24. Keith B. Hengen *et al.*, Neuronal firing rate homeostasis is inhibited by sleep and promoted by wake. *Cell* **165**, 180–191 (2016).
25. S. Ramaswamy, C. Colangelo, H. Markram, Data-driven modeling of cholinergic modulation of neural microcircuits: Bridging neurons, synapses and network activity. *Front. Neural Circuits* **12**, 77–77 (2018).
26. J. M. Miwa *et al.*, Lynx1, an endogenous toxin-like modulator of nicotinic acetylcholine receptors in the mammalian CNS. *Neuron* **23**, 105–114 (1999).
27. H. Morishita *et al.*, Lynx1, a cholinergic brake, limits plasticity in adult visual cortex. *Science* **330**, 1238–1240 (2010).
28. A. E. Takesian *et al.*, Inhibitory circuit gating of auditory critical-period plasticity. *Nat. Neurosci.* **21**, 218–227 (2018).
29. M. Fagiolini *et al.*, Functional postnatal development of the rat primary visual cortex and the role of visual experience: Dark rearing and monocular deprivation. *Vision Res.* **34**, 709–720 (1994).
30. Y. Iwai *et al.*, Rapid critical period induction by tonic inhibition in visual cortex. *J. Neurosci.* **23**, 6695–6702 (2003).
31. D. Whitteridge, The physiology of nerve cells. By J. C. Eccles. Baltimore: The Johns Hopkins Press. 1957. Pp. ix+270. 30s. *Q. J. Exp. Physiol. Cogn. Med. Sci.* **43**, 133–134 (1958).
32. R. Ge, H. Qian, J.-H. Wang, Physiological synaptic signals initiate sequential spikes at soma of cortical pyramidal neurons. *Mol. Brain* **4**, 19–29 (2011).
33. B. W. Connors, S. J. Cruikshank, T. J. Lewis, Synaptic basis for intense thalamocortical activation of feedforward inhibitory cells in neocortex. *Nat. Neurosci.* **10**, 462–468 (2007).
34. J. R. Geiger *et al.*, Relative abundance of subunit mRNAs determines gating and Ca2+ permeability of AMPA receptors in principal neurons and interneurons in rat CNS. *Neuron* **15**, 193–204 (1995).
35. M. Nahmani, A. Erisir, VGluT2 immunochemistry identifies thalamocortical terminals in layer 4 of adult and developing visual cortex. *J. Comp. Neurol.* **484**, 458–473 (2005).
36. G. O. Sipe *et al.*, Microglial P2Y12 is necessary for synaptic plasticity in mouse visual cortex. *Nat. Commun.* **7**, 10905–10905 (2016).
37. B. Miller, L. Chou, B. L. Finlay, The early development of thalamocortical and corticothalamic projections. *J. Comp. Neurol.* **335**, 16–41 (1993).
38. O. Marin, Thalamocortical topography reloaded: It's not where you go, but how you get there. *Neuron* **39**, 388–391 (2003).
39. A. Agmon *et al.*, Topological precision in the thalamic projection to neonatal mouse barrel cortex. *J. Neurosci.* **15**, 549–561 (1995).
40. D. J. Price *et al.*, The development of cortical connections. *Eur. J. Neurosci.* **23**, 910–920 (2006).
41. S. Rumpel, G. Kattenstroth, K. Gottmann, Silent synapses in the immature visual cortex: Layer-specific developmental regulation. *J. Neurophysiol.* **91**, 1097–1101 (2004).
42. R. K. Reh *et al.*, Critical period regulation across multiple timescales. *Proc. Natl. Acad. Sci. U.S.A.* **117**, 23242–23251 (2020).
43. M. Teleńczuk, B. Teleńczuk, A. Destexhe, Modelling unitary fields and the single-neuron contribution to local field potentials in the hippocampus. *J. Physiol.* **598**, 3957–3972 (2020).
44. B. Teleńczuk *et al.*, Local field potentials primarily reflect inhibitory neuron activity in human and monkey cortex. *Sci. Rep.* **7**, 40211–40211 (2017).
45. M. Bazelot *et al.*, Unitary inhibitory field potentials in the CA3 region of rat hippocampus. *J. Physiol.* **588**, 2077–2090 (2010).
46. A. Citri, R. C. Malenka, Synaptic plasticity: Multiple forms, functions, and mechanisms. *Neuropsychopharmacology* **33**, 18–41 (2008).
47. G. G. Turrigiano, The self-tuning neuron: Synaptic scaling of excitatory synapses. *Cell* **135**, 422–435 (2008).
48. M. C. Chang *et al.*, Narp regulates homeostatic scaling of excitatory synapses on parvalbumin-expressing interneurons. *Nat. Neurosci.* **13**, 1090–1097 (2010).
49. H. Hu, J. Gan, P. Jonas, Fast-spiking, parvalbumin+GABAergic interneurons: From cellular design to microcircuit function. *Science.* **345**, 529–529 (2014).
50. J. S. Haas, C. E. Landisman, Bursts modify electrical synaptic strength. *Brain Res.* **1487**, 140–149 (2012).
51. A. Ribic, M. C. Crair, T. Biederer, Synapse-selective control of cortical maturation and plasticity by parvalbumin-autonomous action of SynCAM 1. *Cell Rep.* **26**, 381–393.e6 (2019).
52. G. Faini *et al.*, Perineuronal nets control visual input via thalamic recruitment of cortical PV interneurons. *Elife* **7**, e41520 (2018).
53. K. K. Lensjø *et al.*, Removal of perineuronal nets unlocks juvenile plasticity through network mechanisms of decreased inhibition and increased gamma activity. *J. Neurosci.* **37**, 1269–1283 (2017).

54. K. Kullander, L. Topolnik, Cortical disinhibitory circuits: Cell types, connectivity and function. *Trends Neurosci.* **44**, 643–657 (2021).
55. S. P. Gandhi, Y. Yanagawa, M. P. Stryker, Delayed plasticity of inhibitory neurons in developing visual cortex. *Proc. Natl. Acad. Sci. U.S.A.* **105**, 16797–16802 (2008).
56. R. A. W. Galuske, M. H. J. Munk, W. Singer, Relation between gamma oscillations and neuronal plasticity in the visual cortex. *Proc. Natl. Acad. Sci. U.S.A.* **116**, 23317–23325 (2019).
57. R. Rodriguez *et al.*, Short- and long-term effects of cholinergic modulation on gamma oscillations and response synchronization in the visual cortex. *J. Neurosci.* **24**, 10369–10378 (2004).
58. M. F. Bear, W. Singer, Modulation of visual cortical plasticity by acetylcholine and noradrenaline. *Nature* **320**, 172–176 (1986).
59. T. Toyoizumi *et al.*, A theory of the transition to critical period plasticity: Inhibition selectively suppresses spontaneous activity. *Neuron* **80**, 51–63 (2013).
60. M. A. Whittington *et al.*, Spatiotemporal patterns of gamma frequency oscillations tetanically induced in the rat hippocampal slice. *J. Physiol.* **502**, 591–607 (1997).
61. P. J. Uhlhaas *et al.*, Neural synchrony and the development of cortical networks. *Trends Cogn. Sci.* **14**, 72–80 (2009).
62. L. J. Benoit *et al.*, Adolescent thalamic inhibition leads to long-lasting impairments in prefrontal cortex function. *Nat. Neurosci.* **25**, 714–725 (2022).
63. N. Gogolla *et al.*, Common circuit defect of excitatory-inhibitory balance in mouse models of autism. *J. Neurodev. Disord.* **1**, 172–181 (2009).
64. K. Q. Do, M. Cuenod, T. K. Hensch, Targeting oxidative stress and aberrant critical period plasticity in the developmental trajectory to schizophrenia. *Schizophr. Bull.* **41**, 835–846 (2015).
65. M. S. Olufsen *et al.*, New roles for the gamma rhythm: Population tuning and preprocessing for the Beta rhythm. *J. Comput. Neurosci.* **14**, 33–54 (2003).
66. Z. F. Mainen, T. J. Sejnowski, Influence of dendritic structure on firing pattern in model neocortical neurons. *Nature* **382**, 363–366 (1996).
67. M. M. McCarthy, Quast-et-al-C++_code. Github. https://github.com/mmccart/Quast-et-al-C--code. Deposited 12 November 2022.

Supplementary Information

Supplementary Methods

Mice: All experimental procedures followed the guidelines of the Harvard University and Boston Children's Hospital Institutional Animal Care and Use Committees. C57Bl/6J mice (JAX 000664), PV-GFP mice (1), GAD65-/- mice (2), Lynx1-/- mice (3) were bred in house. All genotypes used were previously backcrossed to produce congenic strains. Mice were given *ad libitum* access to food and water. Mice were maintained on a 12 hr light/dark cycle, with the exception of dark-reared animals, which were born in a dark room and first exposed to light at the start of the experiment.

Monocular Deprivation: Mice were sedated with isoflurane (2% in oxygen) and one eyelid trimmed and sutured shut as previously described (4). For deprivation lasting multiple days, the integrity of the suture was checked daily; mice in which the suture opened and the eye was exposed were discarded from the experiment.

EEG surgery and recording: Mice were anesthetized with isoflurane (2% in oxygen) and prepared for surgery using sterile technique. A small incision was made in the skull and a recording electrode (stainless steel wire, 100 μm diameter, 1 mm exposed tip) slipped between the skull and cortex (recording sites: V1 reference/ground 1 mm posterior to bregma and 2 mm bilaterally from midline, EEG 3 mm lateral of lambda; S1 reference/ground 1.5 mm anterior to bregma and 2 mm bilaterally from lambda, EEG 2 mm lateral of lambda and 1.5 mm posterior to bregma), and the post secured with dental cement. Following at least 4 days of recovery one eye was sutured shut and EEG recording begun 10 minutes following recovery from anesthesia. Recordings were performed in a sound proof box and mice housed in a cylindrical chamber containing bedding, food, hydrogel and nesting material. EEG was recorded for 5 hours with a sampling rate of 256Hz. The EEG signal was filtered through a preamplifier (Pinnacle Technology 8202-SL, high-pass filter 0.5 Hz, x100 gain), run through a humbug to reduce 60 Hz noise contamination, and further amplified (brownlee x20 gain). Data was collected using either VitalRecorder (Kissei) or Sirenia Acquisition (Pinnacle Technology). In some adult mice screws were secured to the skull in place of the wire electrodes.

EEG analysis: Initial EEG data analysis was carried out in Sleep Sign (Kissei). The EEG trace was epoched into 10 second bins, and classified by eye as wake, REM or NREM sleep, with motion artifacts discarded. Power was extracted using Short-Time Fast Fourier Transform for successive 1 minute time segments, for frequencies 1-80 Hz. Data was tapered using the Hann function. Further data analysis was carried out in Matlab (Mathworks). Unless otherwise noted, EEG power from wake epochs was used for analysis. To facilitate comparison between mice, the wake power spectrum was normalized to NREM power. The peak amplitude and frequency represent the maximum point in the power spectrum following normalization and 1/f slope subtraction.

Pharmacological administration: 20 mg/kg diazepam was administered via intraperitoneal injection once a day for three days. Control mice were administered a 1:1 mixture of saline and propylene glycol to match the diazepam solvent (5). Clopidrogel or minocycline (Sigma) were injected intraperiotoneally at 50 mg/kg in saline either 15 or 60 min prior to brief MD.

Eye injections: Mice were anesthetized with 2% isofluorane and injected with 2 μl of a 2% solution of cholera toxin β subunit conjugated with Alexa 488 (Green) or 594 (Red) (Invitrogen, Carlsbad, CA) using a Hamilton® syringe. After 2 days, mice were deeply anesthetized and sliced according to the visual TC protocol. Slices were placed in 4% paraformaldehyde overnight, cryoprotected in 30% sucrose and sub-sectioned to 50 μm on a freezing Vibratome (Leica), maintaining the initial plane.

Slice Preparation: Mice were anesthetized with isoflurane then rapidly decapitated. The brain was removed and placed in an ice-cold choline-based cutting solution (in mM: 78.3 NaCl, 23 NaHCO3, 23 glucose, 33.8 choline chloride, 2.3 KCl, 1.1 NaH2PO3, 6.4 MgCl2, and 0.45 CaCl2) (6). 500 μm thick visual TC slices were sectioned on a vibratome (Microm HM 650V, Thermo Scientific) using a sapphire blade. The visual TC slice was previously described by MacLean et al. (7). Briefly the brain was mounted on a 55 ° agar mold and one 500 μm thick slice was sectioned 300 μm after the disjoining of the corpus callosum. Slices were incubated at 35 °C in oxygenated ACSF (125 mM NaCl, 25 mM glucose, 25 mM NaHCO3, 2.5 mM KCl, 2 mM CaCl2, 1.25 mM NaH2PO4 and 1 mM MgCl2 (310 - 320 mOsm) for at least 15 min, before returning to $20 - 22\,^{\circ}$C.

Voltage Sensitive Dye Imaging (VSDI): VSDI and analysis were performed as previously described (8). Slices were incubated for at least 90 min in the the voltage-sensitive dye Di-4-ANEPPS (Invitrogen; 5 μg/ml in ACSF) before transfer to an ACSF ($20 - 22\,^{\circ}$C) recording chamber. Slices were imaged using an Olympus MVX10 microscope with 4x objective. Excitation light from a shuttered 150 W halogen lamp was band-pass filtered (515 and 535 nm) and reflected toward the sample by a 570-nm dichroic mirror. Emitted fluorescence was long-pass filtered (590 nm) and imaged using a MiCam Ultima CMOS-based camera (SciMedia). A 1 ms stimulating pulse was delivered to the LGN using a bipolar glass stimulating electrode filled with ACSF. Fluorescent changes for a single stimulation trial were collected at 1 ms frame rate for 512 ms and averaged across ten sweeps. Regions of interest containing 5 x 5 pixels covering 125 x 125 μm were spatially integrated using MiCam Ultima analysis software. Individual time course traces were subsequently exported to Igor Pro (WaveMetrics) for custom analysis (8). Fluorescence change was normalized to resting fluorescence (ΔF/F0). Response amplitude was defined as maximum fluorescence change (ΔF/F) per trial at a given region of interest. Variations in daily preparation were normalized by slice; all signals were divided by the change in fluorescence measured in the upper region at a stimulating strength of 0.1 mA.

Acute Slice Electrophysiology: Prior to recording, slices equilibrated for at least 1 hr in oxygenated ACSF before being transferred to a submersion chamber for room temperature recording. Layer 4 non PV or PV cells were targeted by shape and GFP expression using a combination of infrared-Nomarski DIC optics and fluorescent microscopy (Eclipse FNI, 40X immersion objective, Nikon). Recordings were obtained on an Axon MultiClamp 700B amplifier and digitized at 10 kHz (Axon Digidata 1440A). Recording electrodes (2-4MΩ) were fabricated from borosilicate glass microcapillaries (outer diameter, 1.5 mm) with a micropipette puller (DMZ Universal Puller). For whole-cell voltage-clamp recordings the internal solution contained (in mM) 120 Cs-methanesulfonate, 6 CsCl, 2 MgCl2, 0.05 CaCl2, 20 HEPES, 0.02 EGTA, 10 phosphocreatine di(Na) salt, 4 Mg-ATP, 0.4 Na3-GTP, 0.15% biocytin, and 1 lidocaine derivative QX-314 (pH 7.2 with CsOH, 290 - 300 mOsm). Access resistances were maintained at less than 25 MΩ throughout the experiments. TC excitatory post-synaptic currents (EPSCs) were recorded in the presence of 10μM bicuculline. and were stimulated by a bipolar glass stimulating electrode filled with ACSF placed in the LGN or the fiber bundle exiting the LGN. Incremental stimulus intensities were delivered at 0.05 Hz until an evoked EPSC was discernible from failures (6) and a consistent connection was present at a holding potential of -70 mV. TC inputs were differentiated from di-synaptic intracortical inputs on a basis of onset delay ($<$ 9 ms), low jitter and by differences in short term plasticity (9; 10).

Analysis of EPSCs and intrinsic properties was performed using pClamp10 (Molecular Devices). To record AMPA mediated mini EPSCs (mEPSCs), slices were first incubated in ACSF containing 1 μM TTX for 60 minutes prior to recordings and performed in the presence of TTX (1 μM), APV (50 μM) and bicuculline (20 μM). AMPA mEPSCs were recorded for 10 min, high pass filtered at 2 kHz and analyzed using MiniAnalysis (Synaptosoft).

Fos-GFP Single Eye Exposure: MD was performed on the left eye of four Fos-GFP+ mice (c/o Dr. Alison Barth, Carnegie Mellon U) at P22. The mice were then placed in a dark sound chamber to decrease background Fos expression by decreasing light and sound exposure. After three days the mice were exposed to a slow strobe light for 90 min. Mice were perfused transcardially with 0.9% saline followed by 4% paraformaldehyde (PFA). Brains were post-fixed in PFA for 1.5 hours. After fixation the brains were blocked on the TC angle and thinly sliced (50 μm). GFP signal was enhanced with rabbit anti:GFP antibody 1:2000 (Abcam). After determining the boundaries for the various regions, we used ImageJ "particle analysis" function with 0.5-10 μm^2 as the initial parameters to measure the density of Fos labeled cells within each region.

Puncta Immunofluorescence: Mice were perfused transcardially with paraformaldehyde (4% PFA) and the brains removed, postfixed in PFA for 1.5 hours, and cryoprotected in a 30% sucrose solution. Coronal sections (40 μm) were cut on a cryostat or freezing microtome (Leica). Every fourth section was collected and washed in phosphate buffered saline (PBS) for 30 minutes followed by 4 °C overnight incubation in blocking solution (0.8% Triton X- 100 and 20% bovine serum albumin (BSA) in 0.1 M PBS- Triton). Slices were then transferred to a primary antibody solution in 0.2% Triton X-100 and 5% BSA in 0.1 M PBS-Triton for overnight incubation. Antibodies were used at the following concentrations, rabbit anti-GFP 1:2000 (Abcam), rabbit anti-PV 1:1000 (Swant), guinea pig anti-VGluT2 1:500 (Synaptic Systems). After 3 x 15 min washes in PBS-Triton-BSA, sections were incubated overnight in secondary antibody, goat anti-rabbit IgG Alexa 488, goat anti-rabbit IgG Alexa 596, goat anti-guinea pig 564, goat anti mouse 488 or 633 (Invitrogen), diluted at 1:1000 in PBS-Triton-BSA. Sections were washed three times in PBS-Triton for 30 min prior to being mounted on glass slides. The number of VGluT2 immunoreactive puncta surrounding a PV+ cell body were estimated using a custom MatLab script. PV+ positive cells were imaged on a Fluoview FV1000TM scanning microscope (Olympus®) at 100x. Automatic thresholding within MatLab defined the region of the PV+ cell. This region was then used to select a 1.25 μm ring around the neuron. The red VGluT2 channel was thresholded to the median intensity plus 4x the standard deviation and all puncta within the ring, larger than 3 pixels (0.123 μm), were automatically counted and analyzed (Supp Fig. 11).

Statistical Analysis: Population data were expressed as the mean ± SEM. Data were initially analyzed with the Kolmogorov-Smirnov test for normality to guide subsequent analysis. Normally distributed data was analyzed using Student's t test (for two groups) or ANOVA with Tukey's Comparison Test; all other data was analyzed using the Mann-Whitney test (for two groups) or Kruskal-Wallis test with Dunn's Multiple Comparison test. Analysis was done using Prism software (Graphpad, San Diego, CA).

Computational Model

Neurons

The objective of our mathematical models is to suggest possible network activity involved in the generation of MD-induced γ-oscillations and explore the relationship between the emergent γ and decreased thalamocortical AMPA conductance. We construct a thalamocortical network using single-compartment, conductance-based models of layer IV cortical pyramidal cells (PYR), layer IV cortical PV+ interneurons (PV) and thalamocortical cells (TC cells). Neuronal voltages (V) change with time according to a differential equation that equates the capacitive membrane current with the channel currents:

$$c_m \frac{dV}{dt} = -\sum I_{memb} - \sum I_{syn} + I_{app} \tag{1}$$

Membrane voltage (V) is measured in mV. Currents have units in $\mu A/cm^2$. The specific membrane capacitance (c_m) is held at $1 \mu F/cm^2$ for all simulations. The individual collection of membrane and synaptic current, I_{memb} and I_{syn}, respectively, as well as the background excitation term (I_{app}) determine the dynamics of each type of neuron. All neurons contain spiking membrane currents consisting of a fast sodium current (I_{Na}), a fast potassium current (I_K) and a leak current (I_L). The PYR cells also have an M-current (I_M) to account for the spike-frequency adaptation observed in this cell type. We modeled our TC cells during awake, relay states. Thus, the TC cells included only the spiking membrane currents and did not include any low-threshold membrane currents, which are known to play a role in oscillatory activity during sleep and anesthetic states.

All membrane have Hodgkin-Huxley-type conductances formulated as:

$$I = \bar{g} m^n h^k (V - E_{ion}) \tag{2}$$

The maximal conductance of the membrane currents ($\bar{g}$) is held constant, The reversal potential for each current (E_{ion}) is constant and has units of mV. The activation gating variables (m) and inactivation gating variable (h) are unit-less variables between 0 and 1. The number of gating variables is n for the activation gate and k for the inactivation gate. The activation and inactivation gating variables evolve in time according to a two-state kinetic equation formulated (written for the gating variable m) as:

$$\frac{dm}{dt} = \frac{m_\infty - m}{\tau_m} \tag{3}$$

The steady-state function (m_∞) and the time constant of decay (τ_m) can be re-written as rate functions for each current (α_m, β_m) by using the equations:

$$\begin{aligned} m_\infty &= \alpha_m/(\alpha_m + \beta_m) \\ \tau_m &= 1/(\alpha_m + \beta_m). \end{aligned}$$

Models of the spiking currents (I_{Na}, I_K, I_L) for the PYR, PV and TC cells are from (11).

Fast sodium current: The rate functions for the sodium current activation (m) and inactivation (h) variables are formulated as:

$$\begin{aligned} \alpha_m &= \frac{0.32(V+54)}{1 - \exp\left[-(V+54)/4\right]} \\ \beta_m &= \frac{0.28(V+27)}{\exp\left[(V+27)/5\right] - 1} \\ \alpha_h &= 0.128 \exp\left[-(V+50)/18\right] \\ \beta_h &= \frac{4}{1 + \exp\left[-(V+27)/5\right]} \end{aligned}$$

The maximal conductance of the sodium current is $\bar{g}_{Na} = 100mS/cm^2$. The sodium reversal potential is $E_{Na} = 50mV$. The sodium current has three activation gates ($n = 3$) and only one inactivation gate ($k = 1$).

Fast potassium current: The fast potassium current (I_K) has four activation gates ($n = 4$) and no inactivation gates ($k = 0$). The rate functions of the activation gate are described by:

$$\alpha_m = \frac{0.032(V + 52)}{1 - \exp\left[-(V + 52)/5\right]}$$
$$\beta_m = 0.5 \exp\left[-(V + 57)/40\right]$$

The maximal fast potassium channel conductance is $\bar{g}_K = 80mS/cm^2$. The reversal potential for potassium is $E_K = -100mV$.

Leak Current: The leak current (I_L) has no gating variables ($n = 0$, $k = 0$). The maximal conductance of the leak channel is $g_L = 0.1mS/cm^2$. The leak channel reversal potential is $E_L = -67mV$.

M-current: The model of the M-current comes from (12). The M-current has one activation gate ($n = 1$) and no inactivation gate ($k = 0$). The rate functions for the M-current activation gate are described by:

$$\alpha_m = \frac{Q_s 10^{-4}(V + 30)}{1 - \exp\left[-(V + 30)/9\right]}$$
$$\beta_m = -\frac{Q_s 10^{-4}(V + 30)}{1 - \exp\left[(V + 30)/9\right]}$$

We use a Q_{10} factor of 2.3 to scale the rate functions of the M-current since the original formulation of these kinetics described dynamics at 23 °C (12). Thus, for a normal body temperature of 37 °C, the M-current rate equations are scaled by Q_s, which is formulated as:

$$Q_s = Q_{10}^{(37\,^{\circ}\mathrm{C} - 23\,^{\circ}\mathrm{C})/10} = 3.209$$

The maximal M-current conductance is $\bar{g}_m = 1.29mS/cm^2$ for the normal striatum.

Synaptic Connections

Our models contains two types of synaptic currents: AMPA currents (I_{AMPA}) and GABAa currents (I_{GABAa}). Both synaptic currents (I_{syn}) derived from (11) and used Hodgkin-Huxley dynamics formulated as:

$$I_{syn} = \bar{g}s(v_{pre})(V - E_{ion}) \tag{4}$$

Each synaptic current has a single activation gate (s) that depends on the voltage of the pre-synaptic neuron (v_{pre}). E_{ion} is the synaptic reversal potential, and g is the maximal synaptic conductance.

The inhibitory GABAa current is modeled as:

$$I_{GABAa} = \bar{g}_i s_i (V - E_i)$$

The gating variable for inhibitory GABAa synaptic transmission is represented by s_i. For the j^{th} neuron in the network:

$$s_j = \sum_{k=1}^{N} S_{i_k i_j}$$

The variable $S_{i_k i_j}$ describes the kinetics of the gating variable from the k^{th} interneuron to the j^{th} neuron. This variable evolves in time according to:

$$\frac{dS_{i_k i_j}}{dt} = g_{GABAa}(V_k)(1 - S_{i_k i_j}) - \frac{S_{i_k i_j}}{\tau_i}$$

The GABAa time constant of decay (τ_i) is set to 10 ms. The GABAa current reversal potential (E_i) is set to -80 mV in all neurons. The rate functions for the open state of the GABAa receptor ($g_{GABAa}(V_k)$) is described by:

$$g_{GABAa}(V_k) = 2(1 + tanh(\frac{V_k}{4}))$$

The maximal GABAa conductance ($\bar{g}_i$) is 0.03 mS/cm^2 between PV cells within the same population (PVo or PV$_{MD}$) during the critical period and is 0.003 mS/cm^2 in the pre-critical period. The maximal GABAa conductance ($\bar{g}_i$) is 0.25 mS/cm^2 between PV cells of different populations during the critical period and is 0.025 mS/cm^2 in the pre-critical period. The maximal GABAa conductance between PV cells is scaled according to the number of synaptic connections received by a given cell by dividing $\bar{g}_i$ by the number of GABAa synapses made onto that cell. The maximal GABAa conductance ($\bar{g}_i$) from PV cells to PYR cells changes according to plasticity rules (see section entitled “Plasticity Rules”).

The activation gate of AMPA current is described mathematically by the equation:

$$I_{AMPA} = \bar{g}_e s_e (V - E_e)$$

The variable s_e represents the sum of the synaptic activation variables from all excitatory cells projecting to the neuron receiving the AMPA input. For the j^{th} neuron:

$$s_e = \frac{1}{N}\sum_{k=1}^{N} S_{e_k i_j}$$

In this formula, N is the number of excitatory cells that make connections with the j^{th} neuron. The kinetics of the synaptic activation variable from excitatory cell k to neuron j are denoted by $S_{e_k i_j}$ and described by:

$$\frac{dS_{e_k i_j}}{dt} = g_{ee}(V_k)(1 - S_{e_k i_j}) - \frac{S_{e_k i_j}}{\tau_e}$$

The time-constant of decay for the AMPA synapse is $\tau_e = 6ms$ for TC cell synapses onto PYR cells and $\tau_e = 2ms$ for TC cell synapases onto PV cells. The rate function for the open state, $g_{ee}(V_k)$, which is dependent on the membrane voltage of the k^{th} pre-synaptic excitatory cell follows the mathematical formulation:

$$g_{ee}(V_k) = 5(1 + tanh(\frac{V_k}{4}))$$

The maximal AMPA conductance ($\bar{g}_e$) changes with plasticity rules (see "Plasticity Rules" section). The maximal AMPA conductance is scaled according to the number of AMPA synaptic connections received by a given cell by dividing g_e by the number of AMPA synapses made onto that cell. The reversal potential for all AMPA synapses is $E_e = 0mV$.

Gap junction connections were present between all PV cells of the same population (PVo or PV$_{MD}$) during the critical period. These connections were absent during the pre-critical period. The gap junctional current from neuron j to neuron i was modeled as:

$$I_{gap} = \bar{g}_{gap}(V_i - V_j)$$

The maximal gap junction conductance was $\bar{g}_{gap} = 0.01$ mS/cm^2 during the critical period unless otherwise stated.

Networks and LFP

Our networks consist of 40 cells of each type: TC cells, PYR cells and PV cells. All intracortical connections are very weak (silent synapses) initially. In the pre-CP, each PV cell connects weakly to all PYR cells (gGABAa = 0.01 mS/cm^2). These synapses evolved in strength according to the plasticity rules. We originally included weak PYR to PV cell connections. However, since the PYR to PV plasticity rule is bilaterally depressing (13), these synapses remained weak and did not appreciably affect network dynamics. Thus, for the simulations presented in this work, we did not include PYR to PV synapses. Additionally, we did not include excitatory connections between PYR cells. We constructed two populations of PV cells: one receiving TC input relayed from the right eye and the other receiving TC input originating from the left eye (Fig. 6A). Although it is unknown whether PV cells in layer IV of V1 are monocular or binocular, we assumed monocular input based on the literature surrounding ocular dominance columns, which are defined by their selective, monocular input to layer IV. Though ocular dominance columns are not found in mice, we made the assumption that the underlying networks in the binocular zone of mouse V1 resemble ocular dominance columns. Thus, although the neurons in these networks overlap in space, unlike the clear ocular dominance columns present in other mammals, we assumed that the same network principles apply, including monocular input to PV neurons of layer IV of V1. PV cells are connected all-to-all and weakly in the pre-CP. We assume there is greater competition between PV populations than within populations, and thus GABAa conductance is stronger for inhibitory connections between versus within populations (see SI "Synaptic Connections" section for conductance values).

The two TC populations connect to all PV cells in their respective population of PV cells. Thus, each PV cell receives 20 TC inputs. Pyramidal cells receive TC input from all TC cells relayed from both eyes. Initially in the pre-CP, each TC cell connects relatively strongly to one pyramidal cell (gAMPA = 0.12 mS/cm^2) and one PV cell (gAMPA = 0.25 mS/cm^2), and conversely, each PV and PYR cell receives only one strong TC connection. All other TC connections to PYR and PV cells are very weak (silent) (gAMPA = 0.001 mS/cm^2 for weak TC-to-PV synapses and gAMPA = 0.0001 mS/cm^2 for weak TC-to-PYR synapses) (Fig. 6A). We constructed our model with only one strong TC connection to each PV and PYR cell in order to account for the strong topographic organization that is present in the early thalamocortical system (22; 23; 24), the initially sparse innervation of cortex by thalamus (25), as well as the abundance of silent synapses in early networks (26). After initialization, the TC-to-cortex connections evolve according to plasticity rules (see SI section "Synaptic Plasticity Rules").

The CP state is modeled by adding electrical connections between PV cells and strengthening PV-to-PV inhibition (see SI "Synaptic Connections" section for conductance values). At CP onset, PV cells connect electrically with all other PV cells of their own population (those receiving input derived from the right or left eye, respectively), and GABAa connections between all PV cells are strengthened by a factor of 10, since the critical period is accompanied by strengthened inhibition (17).

We model monocular deprivation (MD) by stopping the spiking of half of the TC cells (those receiving input from the deprived eye), which effectively stops the spiking of all PV and pyramidal cells to which those TC cells project strongly. We refer to the population of PV cells deprived of TC input as PV_{MD} cells and to the population of PV cells receiving TC input from the open eye as PVo cells (Fig. 6A).

We model the local field potential (LFP) as the sum of inhibitory currents onto pyramidal cells (19; 20; 21). Spectrograms of the model LFP were obtained using the multitaper power spectral density estimate in MatLab.

We model homeostatic changes due to sleep by decreasing gap junction conductance between PV cells. The maximal PV-to-PV gap junction conductance is lowered from $0.01 mS/cm^2$ to 0.0085 mS/cm^2 after the first period of sleep and to 0.001 mS/cm^2 after the second period of sleep. Sleep is not simulated physiologically since our intent for putting in bouts of "sleep" is solely to demarcate the boundary between two different levels of PV gap junctional conductance as seen in Fig. 7A. As such, "sleep" periods are put in our model by hand by reducing cortical PV spiking by decreasing the maximal sodium conductance of the PV cells to 10 mS/cm^2. This effectively removes all high frequency activity from the simulated LFP.

Background excitation

Only TC cells had a background excitation current: $I_{app} = 0.2$ mS/cm^2. The TC cells also had Gaussian random noise input with an amplitude of $50 \times \sqrt{0.05}$, where 0.05 was the timestep of integration.

Synaptic Plasticity Rules

All AMPA synapses evolve in strength according to a Hebbian spike-time dependent plasticity (STDP) rule (18). The computational formulation of the Hebbian plasticity rule is derived from (14). In particular, we calculate the fractional change in the maximal AMPA conductance ($\omega_{i,j}$) from pre-synaptic cell i to post-synaptic cell j as:

$$\omega_{i,j} = \begin{cases} A_+ e^{-\Delta t/\tau_+} & \text{if } \Delta t \geq 0 \\ -A_- e^{\Delta t/\tau_-} & \text{if } \Delta t < 0 \end{cases} \tag{5}$$

In this equation, Δt is the time of spiking of the post-synaptic cell (t_j) minus time of spiking of the pre-synaptic cell (t_i): $\Delta t = t_j - t_i$. The most recent pre- and post-synaptic spikes are used in this calculation at any given time during the simulation (see “Relaxation of model assumptions” for an alternative method of counting spikes towards plasticity). The amplitude of the fractional synaptic change for potentiation is $A_+ = 0.005$, and the time constant of decay of potentiation is $\tau_+ = 14$ ms. For depression, the amplitude is $A_- = 0.0025$, and the time constant of decay is $\tau_- = 90$ ms (Supp Fig. 5F). We note that the time constant of decay of depression is longer than that used in (14) but still within the range of LTD delays suggested by experiments (15; 16). We model the effect of STDP on the maximal AMPA conductance from cell i to cell j by calculating $\bar{g}_{e_{new}} = \bar{g}_e + \bar{g}_e \cdot \omega_{i,j}$, where $\bar{g}_e$ is the value of the maximal conductance before STDP and $\bar{g}_{e_{new}}$ is the value of the maximal conductance after STDP. The STDP rule is applied after all pre-synaptic spikes and after all post-synaptic spikes.

The PV-to-PYR GABAa synapses evolve in time according to a STDP rule that favors the development of lateral inhibition. The fractional change in the maximal GABAa conductance from pre-synaptic cell i to post-synaptic cell j follows equation (5). The amplitude of the fractional change for the GABAa when $\Delta t \geq 0$ is $A_+ = -0.005$, and the time constant of decay is $\tau_+ = 14$ ms. When $\Delta t < 0$, the amplitude of the fractional change is $A_- = 0.0025$, and the time constant of decay is 34 ms (Supp Fig. 5F).

Computational Tools

Our network models were programmed in C++. The code can be found at: `https://github.com/mmccart/Quast-et-al-C--code`

The differential equations were integrated using a fourth-order Runge-Kutta algorithm. Model output was graphed and analyzed using MatLab. We used the mulittaper method in MatLab to calculate spectral power.

Relaxation of model assumptions

Assumption of GABAa stronger between PV populations than within populations

We assumed GABAa between PV populations is stronger than within PV populations in order to model more competition between than within PV populations. If we relax the assumption of PV inhibition stronger between populations than within populations by decreasing the level of GABAa between populations to the same level as found within populations, we still see the emergence of a 40 Hz γ-oscillation, a rise in the frequency of the γ-rhythm and an eventual fade-out of the γ-oscillation (Supp Fig. 8A). However, in contrast to our original model, a γ-rhythm due to ING dynamics emerges immediately upon entering the CP (Supp Fig. 8A,B) rather emerging only after MD (compare with Fig. 6C), which is inconsistent with the experimental findings in which γ does not emerge during the CP without MD (Fig. 1B,C). This occurs due to the increased excitability of all PV cells after the addition of electrical connections, along with the inability of weak connections between PV populations to suppress the ING in either population. Additionally, different from our original model, after MD the PV$_{MD}$ cells also produce ING, though at a slower γ-frequency than the PVo cells (Supp Fig. 8C,D). As a result of the PV$_{MD}$ ING, a 30 Hz γ-frequency band emerges in the spectrogram along with the 40 Hz band (Supp Fig. 8A). In contrast to the 40 Hz γ-band, the 30 Hz γ-oscillation only emerges after MD (not after CP changes only), it does not increase in frequency as time progresses, and is due to 30 Hz ING in the PV$_{MD}$ population (Supp Fig. 8A-D). The 30 Hz PV$_{MD}$ ING occurs because the weak GABA from PVo to PV$_{MD}$ is insufficient to suppress the additional excitability of the PV$_{MD}$ population due to the presence of electrical connections. The 30 Hz rhythm does not change in frequency over time because no TC-to-PV$_{MD}$ spike-time dependent plasticity can occur in the absence of spiking in the TC cell population that projects to PV$_{MD}$ cells.

In contrast, if we relax our original assumption about connectivity strengths between PV cells by increasing the maximal conductance of GABAa between

PV cells within a population to the same level of GABAa between populations, we no longer see the rise in gamma power (Supp Fig. 8E) or the formation of a clear ING rhythm among the PVo cells (Supp Fig. 8F-H). On the network level, we occasionally see some bouts of synchronous activity among PV cells after MD (Supp Fig. 8G) but these are infrequent and can occur in both PVo and PV_{MD} cell populations. The occasional spiking of PV_{MD} cells after MD occurs due to more inhibition among PVo cells slowing them down such that they provide less inhibition to PV_{MD} cells. Since all PV cells have electrical connections in the CP, which elevates their excitation, PV_{MD} occasionally have enough excitability to spike even in the absence of TC input. However, even with simulations lasting as long as 500 s of simulation time, there is no evidence of ING formation (Supp Fig. 8H). The lack of ING is the result of the increased inhibition between PV cells of the same population, which decreases the excitation of the PV cells not allowing ING to readily form.

Assumption of one-to-one strong TC-to-PV synpases

When one TC-to-PV connection is significantly stronger than the others in the pre-CP, no plasticity occurs in the pre-CP (Supp Fig. 9A,B), no gamma emerges in the pre-CP (Fig. 9C) and network dynamics do not change over the course of the CP (compare Supp Fig. 9D (late pre-CP) and Fig. 6B (early pre-CP)). We relaxed this assumption of strong 1:1 TC-to-PV connectivity in our initial (pre-CP) network by allowing three TC cells to project strongly, with approximately the same strength, to each PV cell in the network, while keeping the rest of the TC-to-PV connections weak. We find that this initial network state allows the TC-to-PV synapses to transition to a more homogeneous state in the pre-CP (Supp Fig 9E,F). Although ING does not emerge due to lack of gap junctions in the pre-CP, broadband power in the model LFP becomes apparent after the TC-to-PV plasticity has taken place (Supp Fig. 9G). As in our CP+MD networks, the evolution of the TC-to-PV synapses to homogeneity results in more excitation to the PV cells, as well as the PV cells responding to the TC population input rather than individual TC cell input (Supp Fig. 9H).

This pre-CP transition occurs because the ongoing competition between the strong synapses continually leaves one of the stronger synapses temporarily weakened, allowing the silent synapses the opportunity to strengthen. Since there is a upper limit to the total amount of excitation a neuron can receive, strengthening silent synapses prevents the weakened strong synapses from strengthening even if the pre-post timing is conducive to LTP. In comparison, when one synapses is significantly stronger than the others, the strong synapses always drives its PV neuron to spike with the pre-post timing that keeps this synapses strong, not allowing the opportunity for other synapses to strengthen. Thus, these results suggest that in order to observe the MD-induced gamma rhythm only during the CP, as seen experimentally, the underlying thalamocortical structure must initially consist of one TC-to-PV connection significantly stronger than the others. Our models suggest this is a necessary condition that allows stable pre-CP dynamics and prevents thalamocortical networks from rewiring TC-to-PV connections to a more homogeneous state before the CP.

Alternative method of spike counting for synaptic plasticity rule

The plasticity rules take into account the most recent pre- and post-synaptic spikes to determine the fractional change in the maximal synaptic conductance. This method works well when pre- and post-synaptic spiking rates are similar. However, if pre- and post-synaptic spiking rates are significantly different, then this method may bias the plasticity towards either LTP or LTD. In our simulations during CP with MD, the PVo cells spike faster than the TCo cells, which could bias the TC-to-PV plasticity towards LTP. Thus, we ran simulations using an unbiased method of counting spikes towards plasticity for the AMPA synapses from TC to PVo. Specifically, this method uses only the PV cell spike immediately before and immediately after each TC cells spike to determine plasticity. With this rule, the number of spikes that contribute to LTP and LTD at the TC-to-PVo synapses are equivalent. With this unbiased method of counting spikes, our results remain qualitatively the same: we observed an abrupt onset of γ with MD that increases in frequency and eventually fades out (Supp Fig. 10A), the strong TC-to-PVo synapses decrease in strength while the initially silent TC-to-PVo synapses increase in strength (Supp Fig. 10B), random spiking in the pre-CP (Supp Fig. 10C) is replaced by ING in the PVo population during the early CP MD state (Supp Fig. 10D). The only difference observed was a longer time for the γ-oscillation to rise in frequency and fade out (compare Supp Fig. 10A using the unbiased counting method and Fig. 6C using the original plasticity counting method).

Supplementary Figures

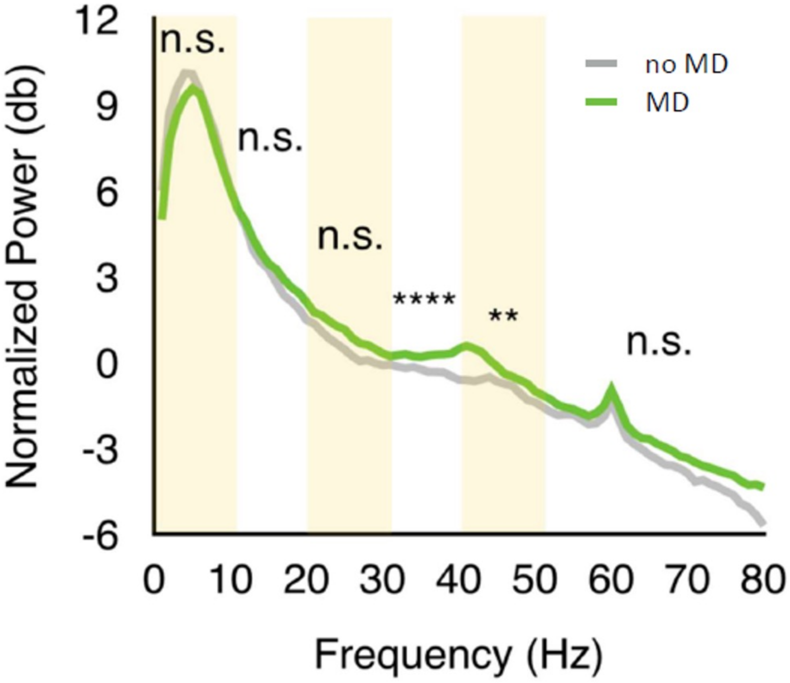

Supp Fig 1: **Monocular deprivation triggers a selective increase in γ power over the visual cortex.**Mean power during the first hour of wake comparing no MD and MD conditions in juvenile mice. Power between the two groups was compared using a Mann Whitney test over the following frequency ranges (in Hz): 1-10, 11-20, 21-30, 31-40, 41-50, 51-80. The only significant differences in power fell in the low gamma range (31-50 Hz). **** $P < 0.0001$, ** $P < 0.01$.

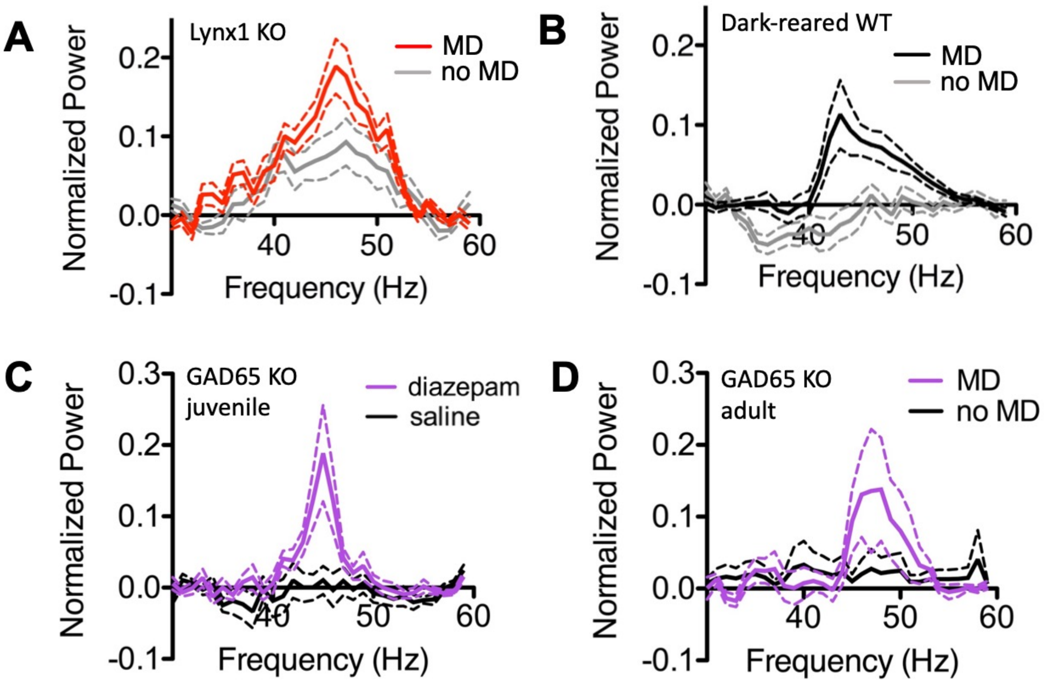

Supp Fig 2: γ **power rise in models of altered CP plasticity.** (A) Mean EEG power of adult Lynx1 KO mice with (red) or without (gray) MD in the γ frequency range for the first hour following MD. (B) Mean EEG power of adult dark reared mice with (black) or without (gray) MD in the γ frequency range for the first hour following MD. (C) Mean EEG power in the γ frequency range for the first hour following MD in Gad65 KO juvenile mice treated with diazepam (light purple) or saline (gray) and Gad65 KO adult mice treated with diazepam (dark purple). Gad65 KO mice treated with diazepam but without MD did not show an increase in γ power (black). EEG power is normalized to NREM γ power, dashed lines show SEM.

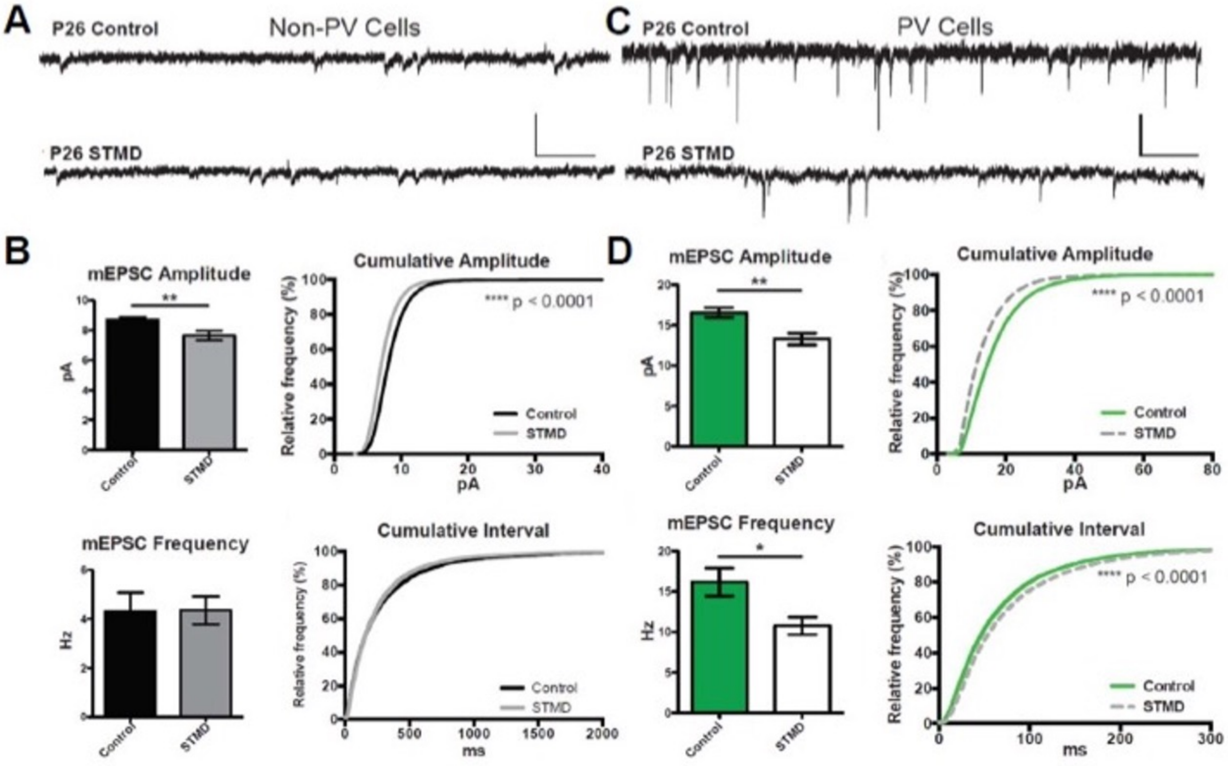

Supp Fig 3: **Thalamocortical synapse strength is reduced following STMD.** (A) Sample mEPSC traces from control P26 mouse (top), and P26 STMD mouse (bottom) from both non-PV and PV cells. Scale bars: 100 ms, 20 pA. (B) There is a small but significant decrease in mean mEPSC amplitude (Student's t test) and (C) right shift in cumulative amplitude in non-PV cells (500-1000 events per cell, Mann-Whitney test; Control n=7, MD n=8). (D) Quantification of significant decrease in mean mEPSC amplitude (Student's t test) and (E) right shift in cumulative amplitude in PV+ cells (1000-1500 events per cell, Mann-Whitney test; Control n=7, MD n=9). There is no significant difference in the mean frequency (F) or cumulative interval (G) for the non-PV cells but a significant decrease in the PV cells (H and I). Bar graph values are mean ± SEM. $^*P<0.05$, $^{**}P<0.01$,$^{****}P<0.0001$.

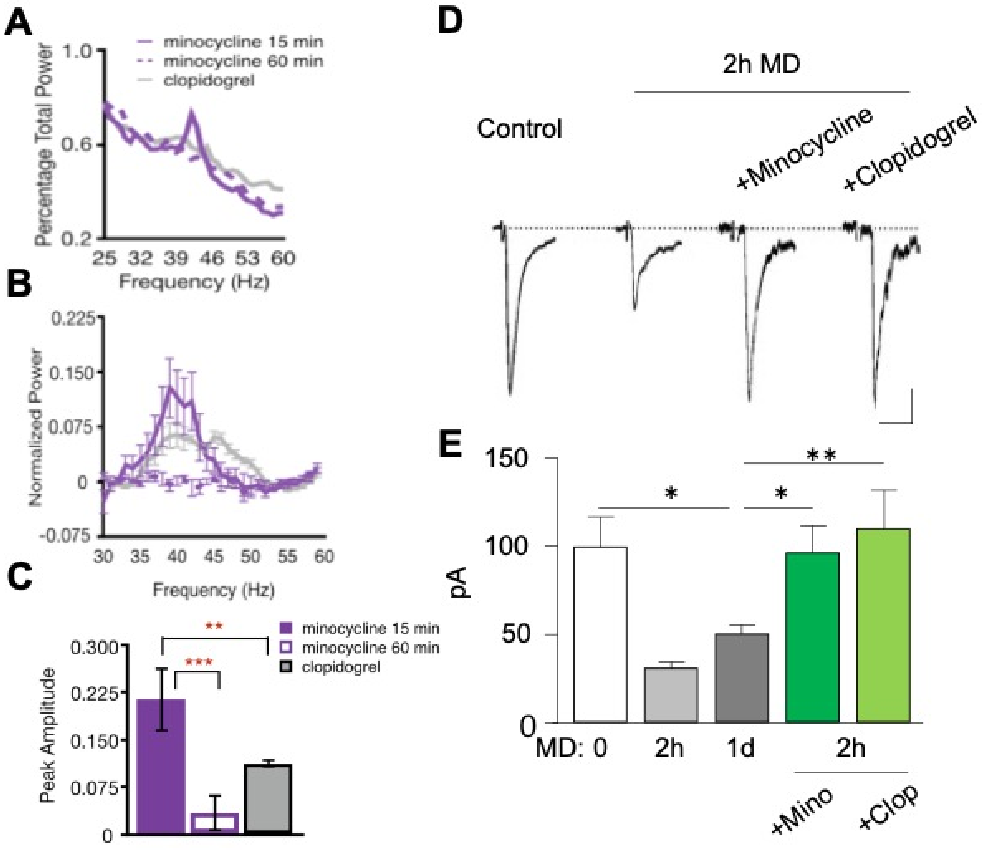

Supp Fig 4: **Microglial inhibitors prevent both rapid g-rhythm induction and TC-to-PV synapse weakening.** (A) Mice received intraperitoneal (i.p.) injections (50mg/kg) of either minocycline or clopidogrel before monocular deprivation (MD). Gamma power peak was curtailed in a time dose-dependent manner, being blocked 1 hour (hollow purple or grey bars, respectively) but not 15 min (solid purple) after treatment. (B) Similarly, both drugs administered 1 hour prior to MD for 2 hours, prevented the loss of thalamocortical input onto PV-cells. N=6 mice each, *P<0.05; **p<0.01; ***p<0.005

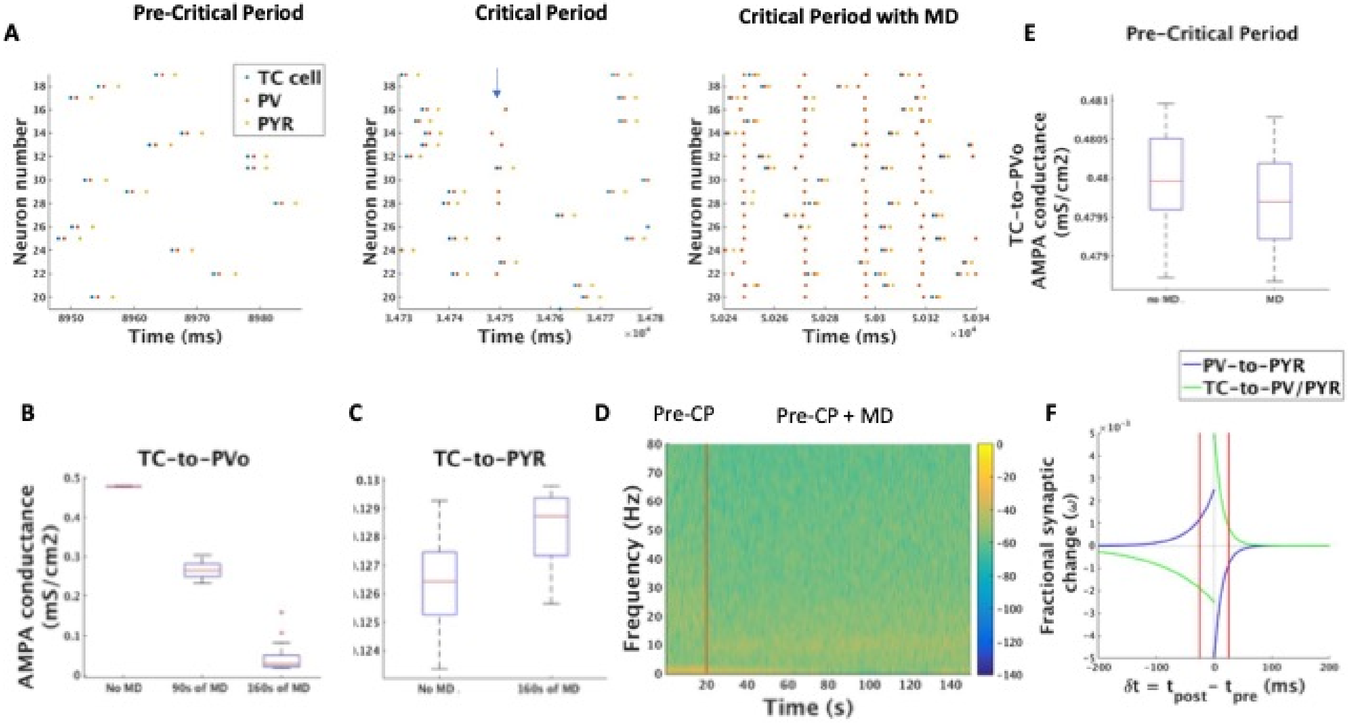

Supp Fig 5: (A) Raster plots of spiking activity of the TC cells, the PVo cells and the PYR cells in the pre-CP, CP and CP MD states. In the pre-CP, the spike timing between the TC cells and the PVo cells is always pre-post for the strong TC-to-PVo synapses. During the CP and during CP MD, spiking between the TC and PVo cells is no longer only pre-post due to synchronous spiking of PVo cells. The blue arrow in the middle raster plot points to a period of time when PVo cells synchronize independent of TC input during the CP. TC to PYR cells remain pre-post under all conditions (pre-CP, CP and CP MD). (B) Boxplots of the AMPA conductance of the strong TC-to-PVo connections during the critical period without MD, as well as during the critical period with MD both at 90s and 160 s of simulation time after the start of MD. (C) Boxplots of the AMPA conductance of the TC-to-PYR connections during the critical period with and without MD after 160 s of simulation time. (D) Spectrogram of the model LFP during the pre-CP before and after MD. Red vertical line marks the start of MD. (E) Boxplots of the TC-to-PVo AMPA conductance before and after MD during the pre-CP. (F) Plasticity rules for model thalamocortical network. STDP from TC cells to either PV or PYR cells follows a Hebbian plasticity rule (green line). STDP from PV cells to PYR cells follows an anti-Hebbian rule that favors the formation of lateral inhibition. Plasticity rules shown out to dt of 200 ms. Red lines mark ±25 ms to show where plasticity occurs during ING.

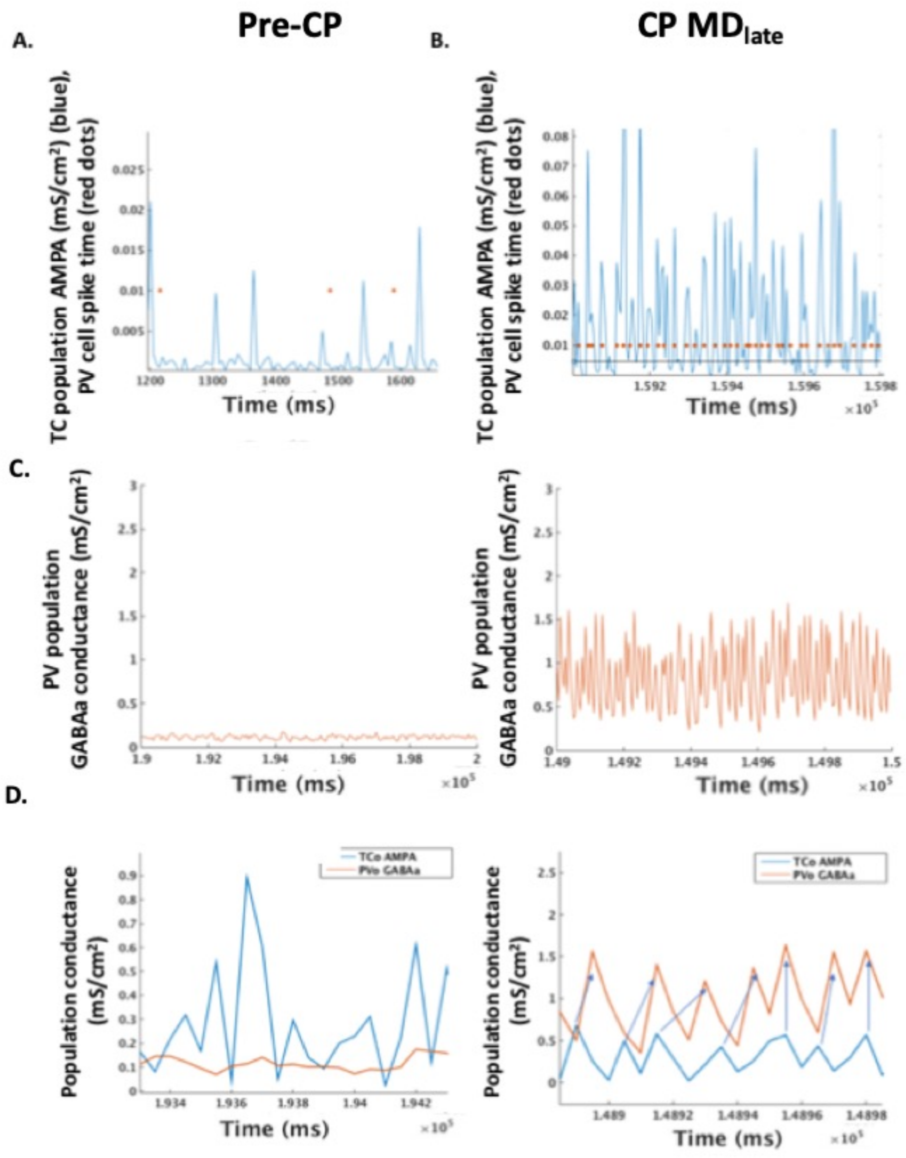

Supp Fig 6: **Network modifications in response to MD during the CP alter network dynamics.** (A) A PV cell does not always spike (red dots) in response to weak population TC AMPA input (blue line) in the pre-CP. (B) The PV cell responds even to weak population TC AMPA input (threshold at 0.005 mS/cm^2, black line) during CP MD$_{late}$ after thalamocortical projections to PV cells become more homogeneous. AMPA conductance represented by blue lines in units of mS/cm^2. Red dots represent times of PV cell spiking. (C) Sum of the GABAa conductance of the population of PVo cells during the pre-CP (left) and during CP MD$_{late}$ after thalamocortical rewiring (right). (D) Sum of the AMPA conductance from the TCo population to the PVo population (blue lines) and sum of the GABAa conductuctance from the PVo population during the pre-CP (left) and after synaptic modifications during CP MD$_{late}$ (right). The arrows show the one-to-one entrainment between the TCo population oscillations and PVo population oscillations during CP MD$_{late}$.

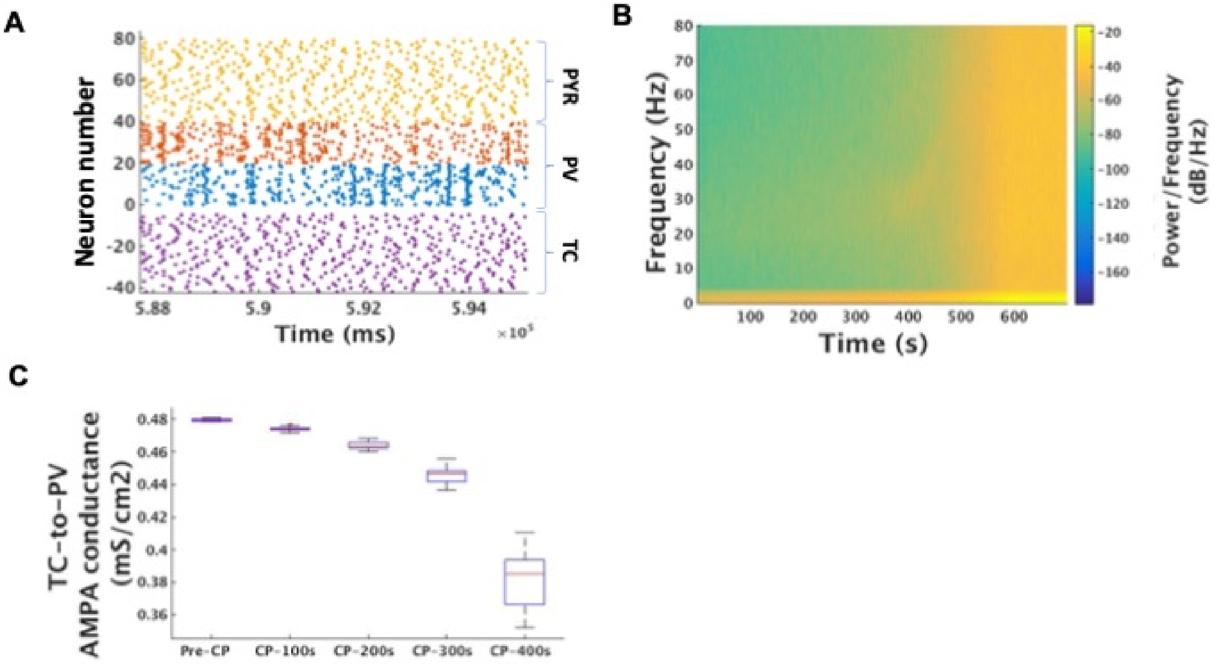

Supp Fig 7: **Critical period dynamics without MD.** (A) Raster plot of all neurons in the thalamocortical network under CP conditions without MD. ING rhythms alternate between the two populations of PV cells (red dots and blue dots). (B) Spectrogram of the model LFP during the CP without MD. Pre-CP simulated from 0 to 20 s, and CP conditions exist after 20 s. (C) Boxplots of the AMPA conductance of the strong TC-to-PV connections during the pre-CP and at simulation time points 100s, 200s, 300s, and 400s after the start of the critical period.

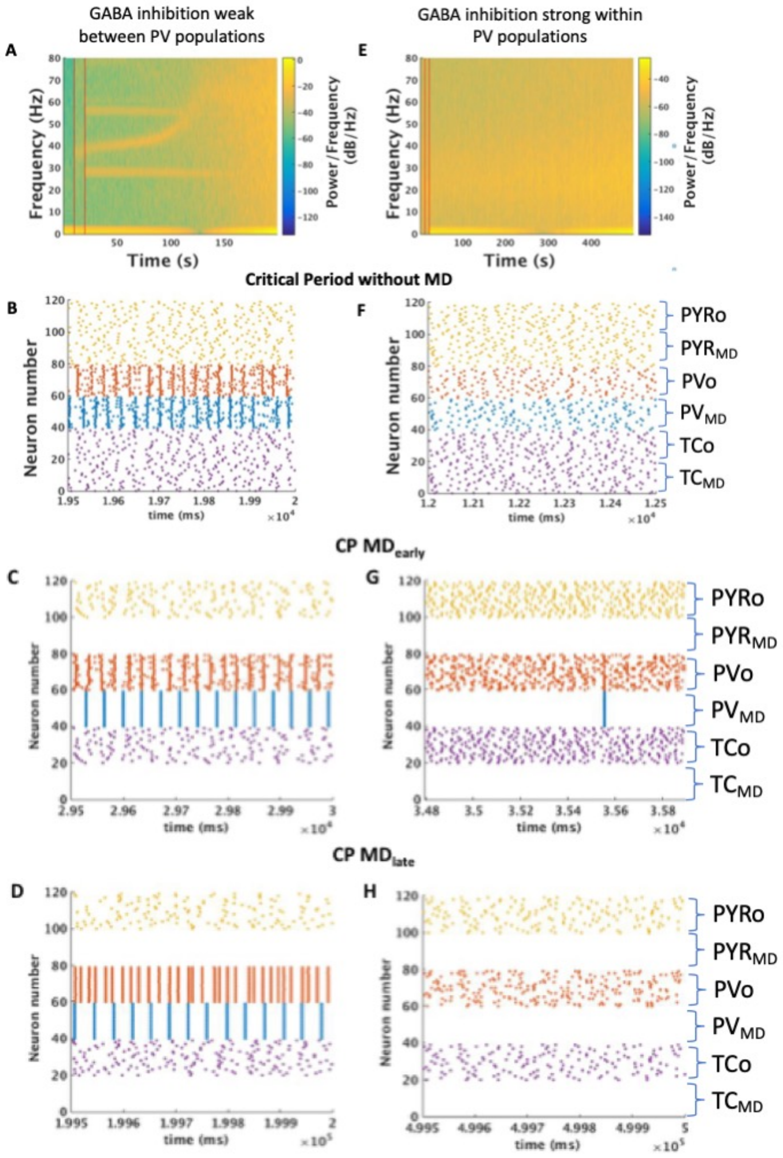

Supp Fig 8: **Network dynamics when GABA conductance used between PV populations equals the GABA conductance used within a PV population.** (A) Spectrogram of model LFP and raster plots of spiking (B) during the CP without MD and (C) during the CP with MD$_{early}$ and (D) during the CP with MD$_{late}$ (last 500 ms of simulation) when gGABA between all PV cells is low (gGABA = 0.03 mS/cm^2 during the CP). (E) Spectrogram of model LFP and raster plots of spiking (F) during the CP without MD (G) during the CP with MD$_{early}$ and (H) during the CP with MD$_{late}$ (last 500 ms of simulation) (H) when gGABA between all PV cells is high (gGABA = 0.25 mS/cm^2 during the CP). Red lines on the spectrogram from left to right mark the transition times between the pre-CP and the CP and between the CP and the CP+MD, respectively.

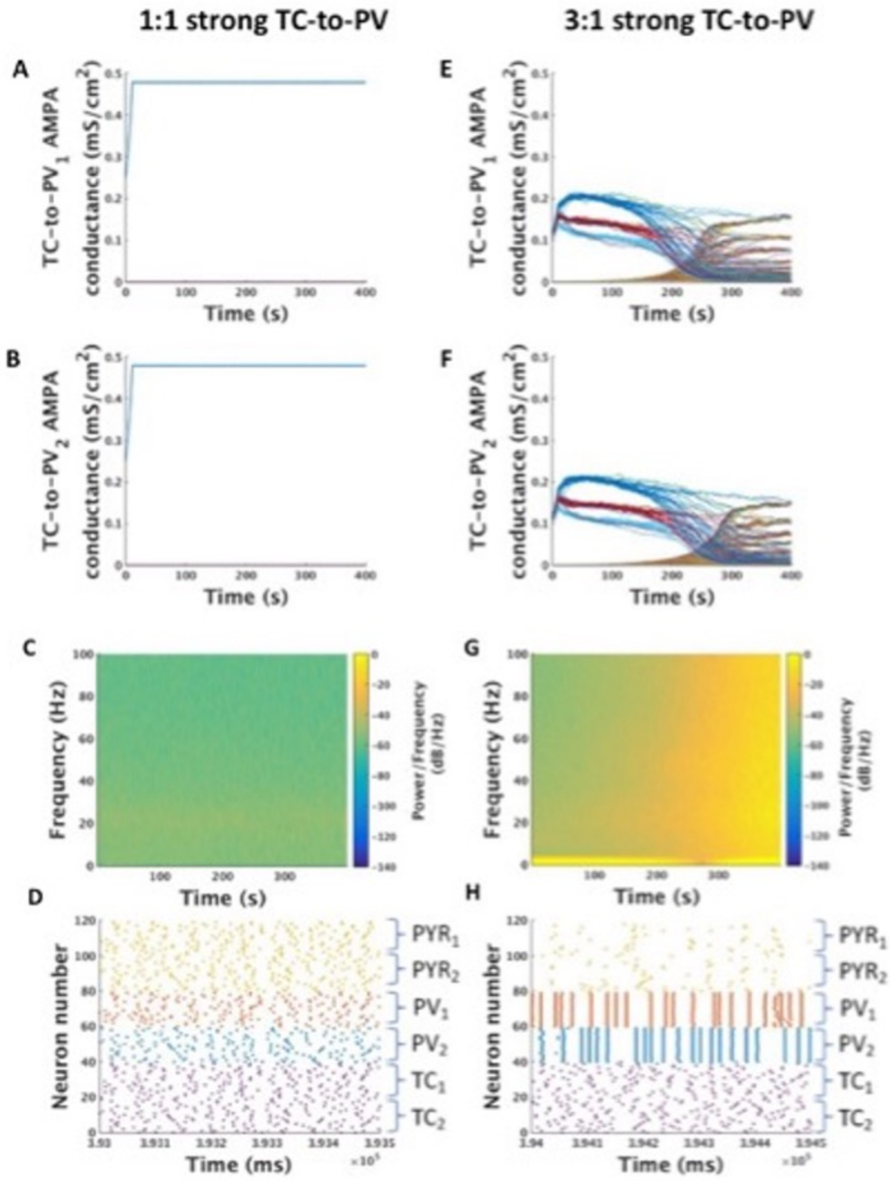

Supp Fig 9: **One-to-one strong TC-to-PV synapses in the pre-CP prevents plasticity.** Evolution of (A) the model TC-to-PV1 synaptic AMPA conductances and (B) the model TC-to-PV2 AMPA conductance throughout the pre-CP when initial TC-to-PV connections are 1:1 strong. PV1 and PV2 are the two populations of PV cells receiving thalamic input originating from the right and left eyes, respectively. (C) Spectrogram of the model LFP during the pre-CP when initial TC-to-PV connections are 1:1 strong. (D) Raster plot of all neurons in the network towards the end of the simulation when initial TC-to-PV connections are 1:1 strong. Evolution of (E) the model TC-to-PV1 synaptic AMPA conductances and (F) the model TC-to-PV2 AMPA conductance throughout the pre-CP when initial TC-to-PV connections are 3:1 strong. (G) Spectrogram of the model LFP during the pre-CP when initial TC-to-PV connections are 3:1 strong. (H) Raster plot of all neurons in the network towards the end of the simulation when initial TC-to-PV connections are 3:1 strong. The subscripts 1 and 2 denote the eye from which the neuron receives its input (in the case of TC cells and PV cells) or its only strong input (in the case of PYR cells).

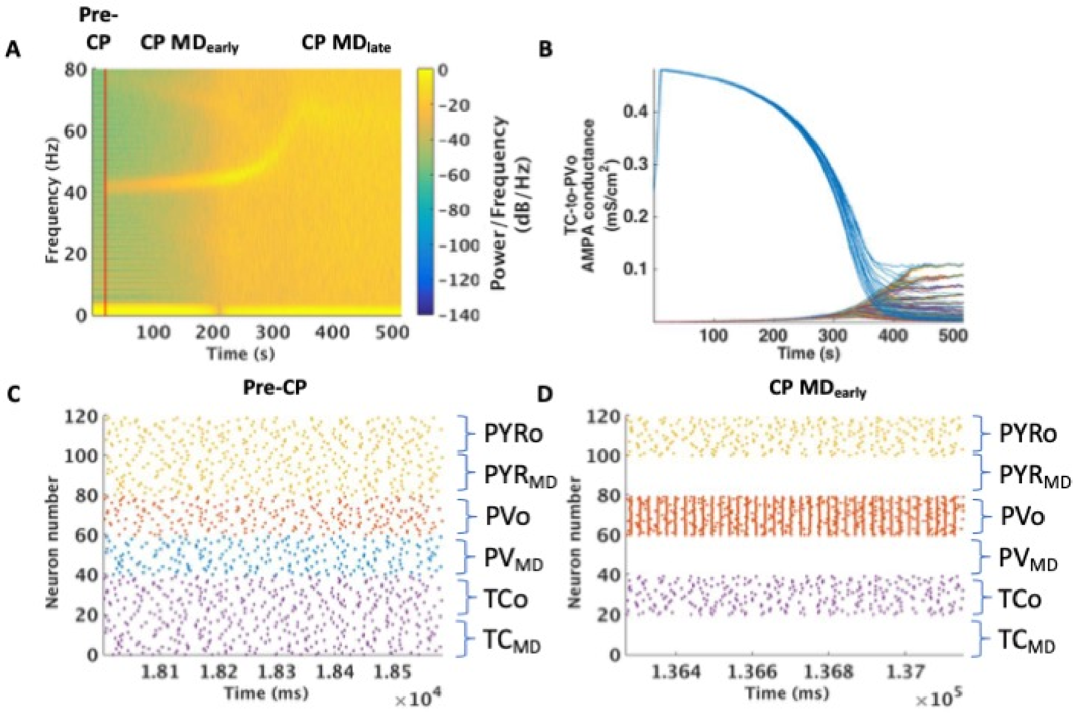

Supp Fig 10: **Network results using an unbiased spike-time counting method.** (A) Spectrogram showing the evolution of gamma in the model LFP during the pre-CP (before red vertical line) and during CP MD$_{early}$ and CP MD$_{late}$. (B) Evolution of all model TC-to-PVo synaptic AMPA conductances during the same time period as shown in (A). Each line shows the AMPA conductance of one TC-to-PVo synapse over time. (C) Representative raster plots of all neurons in the thalamocortical network during the pre-CP and (D) CP MD$_{early}$ states.

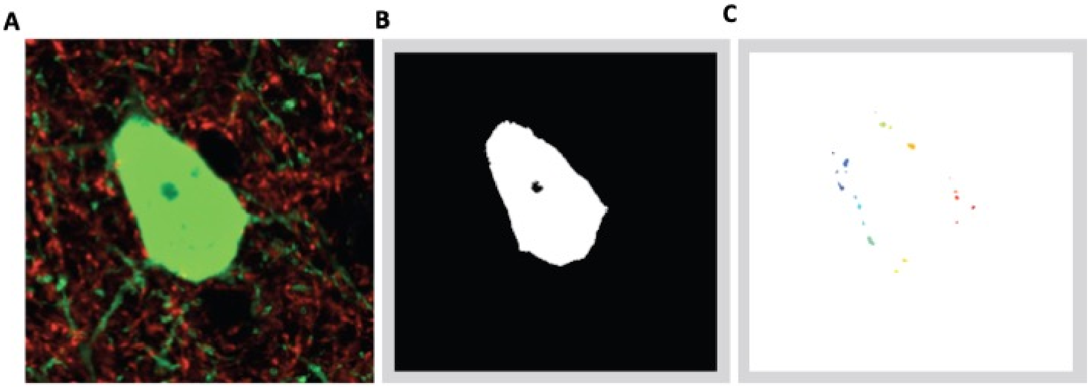

Supp Fig 11: **Automatic Analysis of Synaptic Puncta** (A) Composite image of PV (green) and VGluT2 (red) immunosignal. (B) Automatic thresholding of the green channel to create counting mask. (C) Red channel is segmented based on intensity thresholding (median + 3x S.D.). Counting of puncta restricted within 1.25μm of PV-cell perimeter.

References

[1] Meyer AH, Katona I, Blatow M, Rozov A, Monyer H (2002) In vivo labeling of parvalbumin-positive interneurons and analysis of electrical coupling in identified neurons. J Neurosci 22:7055-7064.

[2] Asada H et al. (1996) Mice lacking the 65 kDa isoform of glutamic acid decarboxylase (GAD65) maintain normal levels of GAD67 and GABA in their brains but are susceptible to seizures. Biochem Biophys Res Commun 229:891-895.

[3] Miwa JM et al. (1999) lynx1, an endogenous toxin-like modulator of nicotinic acetylcholine re-ceptors in the mammalian CNS. Neuron 23:105-114.

[4] Gordon JA, Stryker MP (1996) Experience-dependent plasticity of binocular responses in the primary visual cortex of the mouse. J Neurosci 16:3274-3286.

[5] Takesian AE, Hensch TK. (2013) Balancing plasticity/stability across brain development. Prog Brain Res. 207:3-34.

[6] Hooks BM, Chen C (2006) Distinct roles for spontaneous and visual activity in remodeling of the retinogeniculate synapse. Neuron 52:281-291.

[7] MacLean JN, Watson BO, Aaron GB, Yuste R (2005) Internal dynamics determine the corti-cal response to thalamic stimulation. Neuron 48:811-823.

[8] Barkat TR, Polley DB, Hensch TK (2011) A critical period for auditory TC connectivity. Nat Neurosci 14:1189-1194.

[9] Beierlein M, Gibson JR, Connors BW (2003) Two dynamically distinct inhibitory networks in layer 4 of the neocrtex. J Neurophysiol 90:2987-3000.

[10] Gil Z, Connors BW, Amitai Y (1999) Efficacy of TC and intracortical synaptic connections: quanta, innervation, and reliability. Neuron 23:385-397.

[11] Olufsen MS, Whittington MA, Camperi M, Kopell N (2003) New Roles for the Gamma Rhythm: Population Tuning and Preprocessing for the Beta Rhythm. Journal of Computational Neuroscience 14:33-54.

[12] Mainen ZF, Sejnowski TJ (1996) Influence of dendritic structure on firing pattern in model neocortical neurons. Nature 382:363-366.

[13] Lu, J.T., C.Y. Li, J.P. Zhao, M.M. Poo, and X.H. Zhang, Spike-timing-dependent plasticity of neocortical excitatory synapses on inhibitory interneurons depends on target cell type. J Neurosci, 2007. 27(36): p. 9711-20.

[14] Lee, S., K. Sen, and N. Kopell, Cortical gamma rhythms modulate NMDAR-mediated spike timing dependent plasticity in a biophysical model. PLoS Comput Biol, 2009. 5(12): p. e1000602.

[15] Feldman DE. Timing-based LTP and LTD at vertical inputs to layer II/III pyramidal cells in rat barrel cortex. Neuron. 2000 Jul;27(1):45-56. doi: 10.1016/s0896-6273(00)00008-8. PMID: 10939330.

[16] Debanne D, Gähwiler BH, Thompson SM. Long-term synaptic plasticity between pairs of individual CA3 pyramidal cells in rat hippocampal slice cultures. J Physiol. 1998 Feb 15;507 (Pt 1)(Pt 1):237-47. doi: 10.1111/j.1469-7793.1998.237bu.x. PMID: 9490845; PMCID: PMC2230782.

[17] Reh RK, Dias BG, Nelson CA 3rd, Kaufer D, Werker JF, Kolb B, Levine JD, Hensch TK. Critical period regulation across multiple timescales. Proc Natl Acad Sci U S A. 2020 Sep 22;117(38):23242-23251.

[18] Bi, G. and M. Poo, Synaptic modification by correlated activity: Hebb's postulate revisited. Annu Rev Neurosci, 2001. 24: p. 139-66.

[19] Telenczuk M, Telenczuk B, Destexhe A. Modelling unitary fields and the single-neuron contribution to local field potentials in the hippocampus. J Physiol. 2020 Sep;598(18):3957-3972.

[20] Telenczuk B, Dehghani N, Le Van Quyen M, Cash SS, Halgren E, Hatsopoulos NG, Destexhe A. Local field potentials primarily reflect inhibitory neuron activity in human and monkey cortex. Sci Rep. 2017 Jan 11;7:40211.

[21] Bazelot M, Dinocourt C, Cohen I, Miles R. Unitary inhibitory field potentials in the CA3 region of rat hippocampus. J Physiol. 2010 Jun 15;588(Pt 12):2077-90.

[22] Miller B, Chou L, Finlay BL. The early development of thalamocortical and corticothalamic projections. J Comp Neurol. 1993 Sep 1;335(1):16-41.

[23] Marín O. Thalamocortical topography reloaded: it's not where you go, but how you get there. Neuron. 2003 Jul 31;39(3):388-91.

[24] Agmon A, Yang LT, Jones EG, O'Dowd DK. Topological precision in the thalamic projection to neonatal mouse barrel cortex. J Neurosci. 1995 Jan;15(1 Pt 2):549-61.

[25] Price DJ, et al. (2006) The development of cortical connections. Eur J Neurosci. 23(4):910-20.

[26] Rumpel S, Kattenstroth G, Gottmann K. (2004) Silent synapses in the immature visual cortex: layer-specific developmental regulation. J Neurophysiol. 91(2):1097-101.